Incompatible-mode geometrically non-linear finite element for micropolar elasticity

Sara Grbčić Erdelj, Adnan Ibrahimbegović, Gordan Jelenić

Incompatible-mode geometrically non-linear finite element for micropolar elasticity

Sara Grbčić Erdelj[a], Adnan Ibrahimbegović[b], Gordan Jelenić[a,*]

[a] *University of Rijeka, Faculty of Civil Engineering, Croatia*
[b] *Université de Technologie de Compiègne - Sorbonne Universités, Chair for Computational Mechanics & Insititut Universitaire de France, France*

Abstract

In this work a new three-dimensional geometrically non-linear hexahedral micropolar finite element enhanced with incompatible modes is presented. The analytical model is expressed in terms of Biot-like stress and couple-stress tensors and corresponding Biot-like strain and curvature tensors, with a linear, elastic and isotropic constitutive law. The numerical model is derived based on the principle of virtual work, and the residual derivation together with the linearisation and static condensation procedure is given in detail. The newly developed finite element is tested against the analytical solution of the geometrically non-linear micropolar pure bending problem and the element accuracy and robustness is compared against hexahedral Lagrangian finite elements of first and second order on several numerical examples. It is shown that the newly presented element is fast convergent, more robust and more accurate than the available Lagrangian elements. Moreover, the operator split and static condensation provide for a significantly lower computational cost than standard elements.

Keywords: Micropolar elasticity, Geometrical nonlinearity, Incompatible modes, Large 3D rotations, Pure-bending problem

*Corresponding author
Email addresses: sara.grbcic@uniri.hr (Sara Grbčić Erdelj), adnan.ibrahimbegovic@utc.fr (Adnan Ibrahimbegović), gordan.jelenic@uniri.hr (Gordan Jelenić)

1. Introduction

The so-called size-effect phenomenon observed in experimental analysis of materials with a non-negligible microstructure (e.g. [1], [2], [3]), not taken into account in the classical continuum mechanics, has motivated the research community to come out with extended continuum models. These alternative continuum theories serve as a tool to overcome the limitations imposed by the classical theory, but with a cost of additional degrees of freedom and additional material parameters in the model. Nowadays, a step forward in the development and application of such extended models which would allow an accurate description of modern, manufactured materials such as nanostructured and multilayered materials is of high interest. In the alternative micropolar theory introduced by the Cosserat brothers [4], there exists an independent microrotation field representing the local orientation of a material point, in addition to the displacement field known from the classical continuum theory. Therefore, couple-stress and curvature tensors are also present in the model, leading to six independent material parameters needed to describe such a material [5].

Linear micropolar elasticity has been thoroughly analysed in the theoretical (e.g. [6], [7], [8]) and numerical (e.g. [9], [10], [11], [12]) frameworks in a numerous number of works, where here just a part of the extensive list is given. The theoretical aspects of the non-linear micropolar models has been widely analysed in [13], [14], [15], among many others. On the contrary, as mentioned in [16], in the 3D geometrically non-linear regime the numerical solutions are not broadly present, with two known papers ([17], [18]) dealing with standard three-dimensional finite-element procedures. In addition, it is observed that the geometrically nonlinear finite elements presented in [18] are computationally expensive and fail to converge in certain highly deformed configurations. Consequently, a demand for accurate, robust and inexpensive finite elements persists.

In this work we present a new geometrically non-linear finite element with an incompatible-mode enhancement in the displacement field, while keeping

the microrotation interpolation linear, which can undergo large displacements and large 3D rotations. A special care is taken for the treatment of large 3D rotations, which are not additive and do not commute. Due to the existence of the incompatible-mode parameters, the system of equations is described in terms of three independent vector fields. According to Ibrahimbegović [19], the most convenient solution procedure for this kind of system is the operator split technique which enables separate solution of the equilibrium equations [20], a solution procedure commonly used in computational plasticity. In the present case, the operator split is very efficient, since the extra equation remains linear.

The outcome of the paper is as follows. First, the analytical model of a three-dimensional geometrically non-linear analytical model is presented. Next, the numerical model of a hexahedral geometrically non-linear finite element with enhanced displacement interpolation (using incompatible modes) is derived starting from the principle of virtual work. All the details regarding the complex linearisation and static condensation procedure is given. A step-by-step algorithm implementation is outlined. The newly presented finite element is tested against the analytical solution of a pure bending problem, and its performance, robustness and accuracy is compared against existing geometrically non-linear Lagrangian finite elements of first and second order on several numerical examples.

2. Geometrically non-linear micropolar analytical model

A brief description of the governing equations of a geometrically non-linear micropolar model is given here. A detailed derivation of the model can be found in [21].

Equilibrium equations in material description. In the geometrically non-linear regime, a body, when deformed exhibits large displacements and large rotations, leading to a non-negligible difference between the deformed and undeformed configurations. Here, we choose to express the equilibrium equations in the

so-called material description as

$$\mathrm{DIV}(\mathbf{QB}) + \mathbf{P}_{\mathrm{V}} = \mathbf{0}, \tag{1}$$

$$\mathrm{DIV}(\mathbf{QG}) + \mathrm{ax}(\mathbf{QBF}^{\mathrm{T}} - \mathbf{FB}^{\mathrm{T}}\mathbf{Q}^{\mathrm{T}}) + \mathbf{M}_{\mathrm{V}} = \mathbf{0}, \tag{2}$$

together with the corresponding boundary conditions

$$(\mathbf{QB})\mathbf{N} = \mathbf{P}_{\mathrm{S}} \quad \text{and} \quad (\mathbf{QG})\mathbf{N} = \mathbf{M}_{\mathrm{S}}, \tag{3}$$

where $\mathbf{Q}$ represents the microrotation tensor belonging to the so-called special orthogonal SO(3) Lie group (i.e. $\mathbf{Q}^{-1} = \mathbf{Q}^{\mathrm{T}}$, $\det(\mathbf{Q}) = +1$ and $\mathbf{Q} = \exp\widehat{\boldsymbol{\varphi}}$) where $\widehat{\boldsymbol{\varphi}}$ is a skew-symmetric tensor belonging to the so(3) Lie algebra [22]. The microrotation tensor $\mathbf{Q}$ defines the relation between two sets of orthonormal vectors in the deformed and undeformed configuration, representing the orientation of the material point. In (2), $\mathbf{F} = \mathrm{GRAD}\mathbf{x} = \mathbf{x} \otimes \nabla_X = \mathrm{GRAD}\mathbf{u} + \mathbf{I}$ represents the deformation gradient tensor, $\mathbf{x}$ being the point position vector, ∇_X the partial differential operator (nabla) with respect to the material frame of reference, $\mathbf{u}$ the displacement vector and $\mathbf{I}$ the identity tensor. Also, $\mathbf{B}$ and $\mathbf{G}$ represent the Biot-like stress and Biot-like couple-stress tensor, respectively, while $\mathbf{P}_{\mathrm{V}}$, $\mathbf{M}_{\mathrm{V}}$, $\mathbf{P}_{\mathrm{S}}$, $\mathbf{M}_{\mathrm{S}}$ represent the vectors of body and surface loadings per unit of undeformed volume/area [21], [18].

Non-linear kinematic equations. The non-linear kinematic equations are derived by enforcing the equivalence between the strong form of the equilibrium equations and the principle of virtual work first applied by Reissner on geometrically exact 3D beams [23], leading to

$$\mathbf{E} = \mathbf{Q}^{\mathrm{T}}\mathbf{F} - \mathbf{I}, \tag{4}$$

$$\mathbf{K} = -\frac{1}{2}\boldsymbol{\epsilon} : \left(\mathbf{Q}^{\mathrm{T}}\mathrm{GRAD}\mathbf{Q}\right), \tag{5}$$

where $\mathbf{E}$ represents the Biot-like strain tensor, owing to its resemblance to the standard Biot strain tensor in classical elasticity. Correspondingly, $\mathbf{K}$ represents the Biot-like curvature tensor, while $\boldsymbol{\epsilon}$ is Ricci's alternation tensor. The matemathical operator " : " represents the double contraction product. Both strain and curvature tensors are in general non-symmetric.

Constitutive equations. In this work we focus explicitly on geometrically non-linear effects and keep the constitutive equations linear, which, in the tensor form read

$$\mathbf{B} = \lambda(\text{tr } \mathbf{E})\mathbf{I} + (\mu + \nu)\mathbf{E} + (\mu - \nu)\mathbf{E}^{\mathrm{T}} \tag{6}$$

$$\mathbf{G} = \alpha(\text{tr } \mathbf{K})\mathbf{I} + (\beta + \gamma)\mathbf{K} + (\beta - \gamma)\mathbf{K}^{\mathrm{T}}, \tag{7}$$

with λ and μ as the Lamé constants and $\nu,\ \alpha,\ \beta$ and γ as the additional material parameters taking place in micropolar elasticity.

In other words, the relation between the Biot-like stress tensor and the Biot-like strain tensor is given as $\mathbf{B} = \boldsymbol{\mathcal{T}} : \mathbf{E}$, where the fourth order constitutive tensor $\boldsymbol{\mathcal{T}}$ is equal to

$$\boldsymbol{\mathcal{T}} = \lambda\ \mathbf{I} \otimes \mathbf{I} + (\mu + \nu)\boldsymbol{\mathcal{I}} + (\mu - \nu)\boldsymbol{\mathcal{I}}^{\mathrm{T}}, \tag{8}$$

$\boldsymbol{\mathcal{I}} = \mathbf{e}_i \otimes \mathbf{e}_j \otimes \mathbf{e}_i \otimes \mathbf{e}_j$ being a fourth order identity tensor [18]. The second constitutive equation is likewise equal to $\mathbf{G} = \boldsymbol{\mathcal{D}} : \mathbf{K}$ where the fourth order constitutive tensor $\boldsymbol{\mathcal{D}}$ is equal to

$$\boldsymbol{\mathcal{D}} = \alpha\ \mathbf{I} \otimes \mathbf{I} + (\beta + \gamma)\boldsymbol{\mathcal{I}} + (\beta - \gamma)\boldsymbol{\mathcal{I}}^{\mathrm{T}}. \tag{9}$$

Micropolar parameters $\lambda,\ \mu,\ \nu,\ \alpha,\ \beta,\ \gamma$ can be defined in terms of material parameters consisting of the shear modulus G, Poisson's ratio n, coupling number N, polar ratio ψ and the characteristic lengths for bending and torsion l_b and l_t, via [18]:

$$\begin{gathered} \lambda = \frac{2n\ G}{1-2n}, \qquad \mu = G, \qquad \nu = \frac{G\ N^2}{1-N^2}, \\ \alpha = \frac{2G\ l_t^2(1-\psi)}{\psi}, \quad \beta = G\ l_t^2, \quad \gamma = G(4l_b^2 - l_t^2), \end{gathered} \tag{10}$$

For more details considering the geometrically non-linear micropolar model, together with the additional micropolar material parameters, see [21] and [18].

3. Geometrically nonlinear micropolar hexahedral finite element with incompatible modes

We follow Reissner [23] and start by writing the virtual work principle

$$V_i - V_e = G(\mathbf{u}, \mathbf{Q}; \overline{\mathbf{u}}, \overline{\boldsymbol{\varphi}}) = \int_V \left(\overline{\mathbf{E}} : \mathbf{B} + \overline{\mathbf{K}} : \mathbf{G}\right) dV - \int_V \left(\overline{\mathbf{u}} \cdot \mathbf{P}_{\mathrm{V}} + \overline{\boldsymbol{\varphi}} \cdot \mathbf{M}_{\mathrm{V}}\right) dV - \int_{S_p} \left(\overline{\mathbf{u}} \cdot \mathbf{P}_{\mathrm{S}} + \overline{\boldsymbol{\varphi}} \cdot \mathbf{M}_{\mathrm{S}}\right) dS = 0.$$

where we introduce the virtual strain and curvature tensors which follow from (4) and (5) as

$$\overline{\mathbf{E}} = \mathbf{Q}^{\mathrm{T}}(\mathrm{GRAD}\overline{\mathbf{u}} + \widehat{\overline{\boldsymbol{\varphi}}}^{\mathrm{T}}\mathbf{F}), \tag{11}$$

$$\overline{\mathbf{K}} = \mathbf{Q}^{\mathrm{T}}\mathrm{GRAD}\overline{\boldsymbol{\varphi}}. \tag{12}$$

The virtual work equation can thus be written as

$$G(\mathbf{u}, \mathbf{Q}, \overline{\mathbf{u}}, \overline{\boldsymbol{\varphi}}) = \int_V \left((\mathbf{Q}^{\mathrm{T}}\mathrm{GRAD}\overline{\mathbf{u}}) : \mathbf{B} + (\mathbf{Q}^{\mathrm{T}}\widehat{\overline{\boldsymbol{\varphi}}}^{\mathrm{T}}\mathbf{F}) : \mathbf{B} + (\mathbf{Q}^{\mathrm{T}}\mathrm{GRAD}\overline{\boldsymbol{\varphi}}) : \mathbf{G}\right) dV - \int_V \left(\overline{\mathbf{u}} \cdot \mathbf{P}_{\mathrm{V}} + \overline{\boldsymbol{\varphi}} \cdot \mathbf{M}_{\mathrm{V}}\right) dV - \int_{S_p} \left(\overline{\mathbf{u}} \cdot \mathbf{P}_{\mathrm{S}} + \overline{\boldsymbol{\varphi}} \cdot \mathbf{M}_{\mathrm{S}}\right) dS = 0, \tag{13}$$

where a superimposed bar is used to represent virtual fields. The domain is chosen to be discretised using isoparametric hexahedral finite elements with eight nodes with numbering convention as shown in Figure 1.

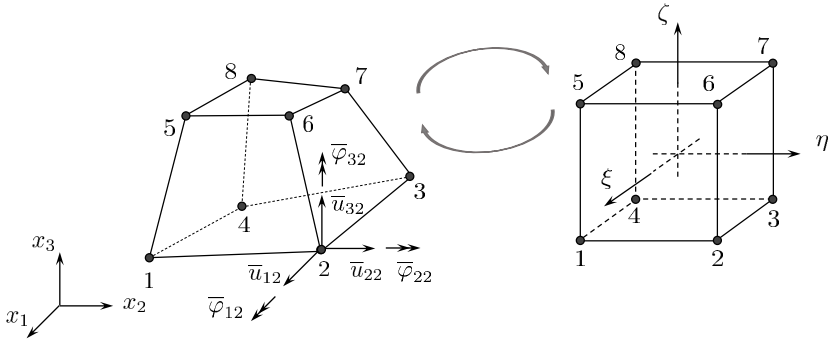

Figure 1: Isoparametric hexahedral finite element with 8 nodes: real element in physical space (left), parent element in natural coordinates (right)

In order to obtain the residual load vector, the virtual kinematic fields have to be approximated using chosen interpolations. The key idea is to choose the virtual displacement interpolation enhanced with the so-called incompatible modes, as follows:

$$\overline{\mathbf{u}}^h = \sum_{i=1}^{8} N_i(\xi,\eta,\zeta)\overline{\mathbf{u}}_i^e + \sum_{i=1}^{3} M_i(\xi,\eta,\zeta)\overline{\boldsymbol{\alpha}}_i^e, \tag{14}$$

where

$$N_i(\xi,\eta,\zeta) = \frac{1}{8}(1+\xi_a\xi)(1+\eta_a\eta)(1+\zeta_a\zeta),\ \ \xi_a = \pm 1,\ \eta_a = \pm 1,\ \zeta_a = \pm 1,\ i = 1,..,8, \tag{15}$$

represent the Lagrange trilinear isoparametric shape functions, $\overline{\mathbf{u}}_i^e = \langle \overline{u}_{1i}\ \overline{u}_{2i}\ \overline{u}_{3i}\rangle^{\mathrm{T}}$ is the vector of element virtual nodal displacements at node i, and $\overline{\boldsymbol{\alpha}}_i^e = \langle \overline{\alpha}_{1i}\ \overline{\alpha}_{2i}\ \overline{\alpha}_{3i}\rangle^{\mathrm{T}}$ is the vector of the element virtual parameters for the incompatible shape functions chosen as: $M_1 = 1-\xi^2,\ M_2 = 1-\eta^2$, and $M_3 = 1-\zeta^2$. From (14) we can see that the displacement field interpolation consists of the conventional (compatible) part and the enhanced (incompatible) part. The choice of incompatible part as quadratic polynomials is made to complete the basis, which ensures higher accuracy of 8-node hexahedron. We note in passing that one can also enhance 27-node element with cubic polynomials in the same manner as described in [24].

The virtual microrotation field is interpolated by using only the standard Lagrange interpolation:

$$\overline{\boldsymbol{\varphi}}^h = \sum_{i=1}^{8} N_i(\xi,\eta,\zeta)\ \overline{\boldsymbol{\varphi}}_i^e, \tag{16}$$

where $\overline{\boldsymbol{\varphi}}_i^e = \langle \overline{\varphi}_{1i}\ \overline{\varphi}_{2i}\ \overline{\varphi}_{3i}\rangle^{\mathrm{T}}$ is the vector of virtual nodal microrotations at node i. For simplicity, first we analyse the first integral of equation (13) where we introduce the interpolation of the virtual fields and apply tensor identities defined in Appendix B of [18] to obtain

$$\int_V \Big((\mathbf{Q}^{\mathrm{T}}\mathrm{GRAD}\overline{\mathbf{u}}) : \mathbf{B} + (\mathbf{Q}^{\mathrm{T}}\widehat{\overline{\boldsymbol{\varphi}}}^{\mathrm{T}}\mathbf{F}) : \mathbf{B} + (\mathbf{Q}^{\mathrm{T}}\mathrm{GRAD}\overline{\boldsymbol{\varphi}}) : \mathbf{G} \Big) \, dV =$$
$$\int_V \left(\sum_{i=1}^{8} \overline{\mathbf{u}}_i^{e^{\mathrm{T}}} \mathbf{QB}(N_i \nabla_X) + \sum_{a=1}^{3} \overline{\boldsymbol{\alpha}}_a^{e^{\mathrm{T}}} \mathbf{QB}(M_a \nabla_X) + \sum_{i=1}^{8} \overline{\boldsymbol{\varphi}}_i^{e^{\mathrm{T}}} 2N_i \mathrm{ax}\left(\mathrm{skew}\left(\mathbf{F}\mathbf{B}^{\mathrm{T}}\mathbf{Q}^{\mathrm{T}}\right)\right) + \right.$$
$$\left. \sum_{i=1}^{8} \overline{\boldsymbol{\varphi}}_i^{e^{\mathrm{T}}} \mathbf{QG}(N_i \nabla_X) \right) dV, \tag{17}$$

where the operator $\mathrm{ax}\left(\mathrm{skew}\left(\bullet\right)\right)$ gives the axial vector of a skew-symmetric matrix. By substituting equation (17) in (13), and grouping terms multiplying the corresponding virtual kinematic fileds we obtain

$$\begin{aligned}
\mathbb{A}_{e=1}^{nel} \int_V & \left(\sum_{i=1}^{8} \left\langle \overline{\mathbf{u}}_i^{e^{\mathrm{T}}} \quad \overline{\boldsymbol{\varphi}}_i^{e^{\mathrm{T}}} \right\rangle \begin{Bmatrix} \mathbf{QB}(N_i \nabla_X) \\ 2N_i \mathrm{ax}\left(\mathrm{skew}\left(\mathbf{F}\mathbf{B}^{\mathrm{T}}\mathbf{Q}^{\mathrm{T}}\right)\right) + \mathbf{QG}(N_i \nabla_X) \end{Bmatrix} \right) dV \\
& + \int_V \left(\sum_{a=1}^{3} \overline{\boldsymbol{\alpha}}_a^{e^{\mathrm{T}}} \mathbf{QB}(M_a \nabla_X) \right) dV \\
& - \int_V \left(\sum_{i=1}^{8} \left\langle \overline{\mathbf{u}}_i^{e^{\mathrm{T}}} \quad \overline{\boldsymbol{\varphi}}_i^{e^{\mathrm{T}}} \right\rangle N_i \begin{Bmatrix} \mathbf{P}_{\mathrm{V}} \\ \mathbf{M}_{\mathrm{V}} \end{Bmatrix} + \sum_{a=1}^{3} \overline{\boldsymbol{\alpha}}_a^{e^{\mathrm{T}}} M_a \mathbf{P}_{\mathrm{V}} \right) dV \\
& - \int_{S_p} \left(\sum_{i=1}^{8} \left\langle \overline{\mathbf{u}}_i^{e^{\mathrm{T}}} \quad \overline{\boldsymbol{\varphi}}_i^{e^{\mathrm{T}}} \right\rangle N_i \begin{Bmatrix} \mathbf{P}_{\mathrm{S}} \\ \mathbf{M}_{\mathrm{S}} \end{Bmatrix} + \sum_{a=1}^{3} \overline{\boldsymbol{\alpha}}_a^{e^{\mathrm{T}}} M_a \mathbf{P}_{\mathrm{S}} \right) dS = 0,
\end{aligned} \tag{18}$$

for any virtual parameters. Next, we introduce the vector of virtual element nodal degrees of freedom as $\overline{\mathbf{d}}^e = \langle \overline{\mathbf{d}}_1^e \ \overline{\mathbf{d}}_2^e \ \ldots \ \overline{\mathbf{d}}_8^e \rangle^{\mathrm{T}}$, where $\overline{\mathbf{d}}_i^e = \langle \overline{\mathbf{u}}_i^e \ \overline{\boldsymbol{\varphi}}_i^e \rangle^{\mathrm{T}} = \langle \overline{u}_{1i} \ \overline{u}_{2i} \ \overline{u}_{3i} \ \overline{\varphi}_{1i} \ \overline{\varphi}_{2i} \ \overline{\varphi}_{3i} \rangle^{\mathrm{T}}$, i being the node number, giving

$$\begin{aligned}
& \mathbb{A}_{e=1}^{nel} \sum_{i=1}^{8} \overline{\mathbf{d}}_i^{e^{\mathrm{T}}} \int_V \begin{Bmatrix} \mathbf{QB}(N_i \nabla_X) \\ 2N_i \mathrm{ax}\left(\mathrm{skew}\left(\mathbf{F}\mathbf{B}^{\mathrm{T}}\mathbf{Q}^{\mathrm{T}}\right)\right) + \mathbf{QG}(N_i \nabla_X) \end{Bmatrix} dV + \sum_{a=1}^{3} \overline{\boldsymbol{\alpha}}_a^{e^{\mathrm{T}}} \int_V \mathbf{QB}(M_a \nabla_X) dV \\
& - \sum_{i=1}^{8} \overline{\mathbf{d}}_i^{e^{\mathrm{T}}} \int_V N_i \begin{Bmatrix} \mathbf{P}_{\mathrm{V}} \\ \mathbf{M}_{\mathrm{V}} \end{Bmatrix} dV - \sum_{a=1}^{3} \overline{\boldsymbol{\alpha}}_a^{e^{\mathrm{T}}} \int_V M_a \mathbf{P}_{\mathrm{V}} dV - \sum_{i=1}^{8} \overline{\mathbf{d}}_i^{e^{\mathrm{T}}} \int_{S_p} N_i \begin{Bmatrix} \mathbf{P}_{\mathrm{S}} \\ \mathbf{M}_{\mathrm{S}} \end{Bmatrix} dS \\
& - \sum_{a=1}^{3} \overline{\boldsymbol{\alpha}}_a^{e^{\mathrm{T}}} \int_{S_p} M_a \mathbf{P}_{\mathrm{S}} dS = 0,
\end{aligned} \tag{19}$$

or written in an expanded form

$$\mathbb{A}_{e=1}^{nel}\left(\langle \overline{\mathbf{d}}_1^{e^{\mathrm{T}}}\ \overline{\mathbf{d}}_2^{e^{\mathrm{T}}}\ \ldots\ \overline{\mathbf{d}}_8^{e^{\mathrm{T}}}\rangle \int_V \left\{ \begin{bmatrix} \mathbf{QB}(N_1\nabla_X) \\ 2N_1 \mathrm{ax}\left(\mathrm{skew}\left(\mathbf{FB}^{\mathrm{T}}\mathbf{Q}^{\mathrm{T}}\right)\right) + \mathbf{QG}(N_1\nabla_X) \end{bmatrix} \right.\right.$$
$$\left.\left. \begin{bmatrix} \mathbf{QB}(N_2\nabla_X) \\ 2N_2 \mathrm{ax}\left(\mathrm{skew}\left(\mathbf{FB}^{\mathrm{T}}\mathbf{Q}^{\mathrm{T}}\right)\right) + \mathbf{QG}(N_2\nabla_X) \end{bmatrix} \right.\right.$$
$$\left.\left. \begin{bmatrix} ... \end{bmatrix} \right.\right.$$
$$\left.\left. \begin{bmatrix} \mathbf{QB}(N_8\nabla_X) \\ 2N_8 \mathrm{ax}\left(\mathrm{skew}\left(\mathbf{FB}^{\mathrm{T}}\mathbf{Q}^{\mathrm{T}}\right)\right) + \mathbf{QG}(N_8\nabla_X) \end{bmatrix} \right\} dV \right)$$
$$- \langle \overline{\mathbf{d}}_1^{e^{\mathrm{T}}}\ \overline{\mathbf{d}}_2^{e^{\mathrm{T}}}\ \ldots\ \overline{\mathbf{d}}_8^{e^{\mathrm{T}}}\rangle \int_V \left\{ \begin{matrix} N_i \begin{bmatrix} \mathbf{P}_{\mathrm{V}} \\ \mathbf{M}_{\mathrm{V}} \end{bmatrix} \\ N_i \begin{bmatrix} \mathbf{P}_{\mathrm{V}} \\ \mathbf{M}_{\mathrm{V}} \end{bmatrix} \\ \begin{bmatrix} ... \end{bmatrix} \\ N_i \begin{bmatrix} \mathbf{P}_{\mathrm{V}} \\ \mathbf{M}_{\mathrm{V}} \end{bmatrix} \end{matrix} \right\} dV - \langle \overline{\mathbf{d}}_1^{e^{\mathrm{T}}}\ \overline{\mathbf{d}}_2^{e^{\mathrm{T}}}\ \ldots\ \overline{\mathbf{d}}_8^{e^{\mathrm{T}}}\rangle \int_{Sp} \left\{ \begin{matrix} N_i \begin{bmatrix} \mathbf{P}_{\mathrm{S}} \\ \mathbf{M}_{\mathrm{S}} \end{bmatrix} \\ N_i \begin{bmatrix} \mathbf{P}_{\mathrm{S}} \\ \mathbf{M}_{\mathrm{S}} \end{bmatrix} \\ \begin{bmatrix} ... \end{bmatrix} \\ N_i \begin{bmatrix} \mathbf{P}_{\mathrm{S}} \\ \mathbf{M}_{\mathrm{S}} \end{bmatrix} \end{matrix} \right\} dS$$
$$+ \langle \overline{\boldsymbol{\alpha}}_1^{e^{\mathrm{T}}}\ \overline{\boldsymbol{\alpha}}_2^{e^{\mathrm{T}}}\ \overline{\boldsymbol{\alpha}}_3^{e^{\mathrm{T}}}\rangle \int_V \left\{ \begin{matrix} \mathbf{QB}(M_1\nabla_X) \\ \mathbf{QB}(M_2\nabla_X) \\ \mathbf{QB}(M_3\nabla_X) \end{matrix} \right\} dV$$
$$- \langle \overline{\boldsymbol{\alpha}}_1^{e^{\mathrm{T}}}\ \overline{\boldsymbol{\alpha}}_2^{e^{\mathrm{T}}}\ \overline{\boldsymbol{\alpha}}_3^{e^{\mathrm{T}}}\rangle \left(\int_V \left\{ \begin{matrix} M_1\mathbf{P}_{\mathrm{V}} \\ M_2\mathbf{P}_{\mathrm{V}} \\ M_3\mathbf{P}_{\mathrm{V}} \end{matrix} \right\} dV + \int_{Sp} \left\{ \begin{matrix} M_1\mathbf{P}_{\mathrm{S}} \\ M_2\mathbf{P}_{\mathrm{S}} \\ M_3\mathbf{P}_{\mathrm{S}} \end{matrix} \right\} dS \right) \right) = 0, \tag{20}$$

Here we recognise that (20) has to hold true for arbitrary virtual parameters leading to the element residual force vector $\mathbf{g}^e$ and the element incompatible-mode residual vector $\mathbf{g}^{e,\alpha}$ as

$$\mathbb{A}_{e=1}^{nel}\left(\overline{\mathbf{d}}^{e^{\mathrm{T}}}\mathbf{g}^e + \overline{\boldsymbol{\alpha}}^{e^{\mathrm{T}}}\mathbf{g}^{e,\alpha}\right) = \mathbb{A}_{e=1}^{nel}\left(\overline{\mathbf{d}}^{e^{\mathrm{T}}}(\mathbf{q}^{int,e} - \mathbf{q}^{ext,e}) + \overline{\boldsymbol{\alpha}}^{e^{\mathrm{T}}}(\mathbf{q}^{int,e,\alpha} - \mathbf{q}^{ext,e,\alpha})\right) = \mathbf{0}, \tag{21}$$

where $\mathbf{q}^{int,e}$ represents the element vector of internal forces, $\mathbf{q}^{ext,e}$ represents the element vector of external forces and $\mathbf{g}^{e,\alpha}$ represents the element incompatible-

mode residual vector with $\mathbf{q}^{int,e,\alpha}$ as the internal-force incompatible-mode vector and $\mathbf{q}^{ext,e,\alpha}$ as the external-force incompatible-mode vector.

The element internal-force vector at node i is thus equal to

$$\mathbf{q}_i^{int,e} = \int_V \begin{Bmatrix} \mathbf{QB}(N_i\nabla_X) \\ 2N_i \mathrm{ax}(\mathrm{skew}(\mathbf{F}\mathbf{B}^{\mathrm{T}}\mathbf{Q}^{\mathrm{T}})) + \mathbf{QG}(N_i\nabla_X) \end{Bmatrix} dV, \tag{22}$$

while the element incompatible-mode residual vector $\mathbf{g}^{e,\alpha}$ is equal to

$$\mathbf{g}^{e,\alpha} = \mathbf{q}^{int,e,\alpha} - \mathbf{q}^{ext,e,\alpha}, \tag{23}$$

where

$$\mathbf{q}^{int,e,\alpha} = \int_V \begin{Bmatrix} \mathbf{QB}(M_1\nabla_X) \\ \mathbf{QB}(M_2\nabla_X) \\ \mathbf{QB}(M_3\nabla_X) \end{Bmatrix} dV, \qquad \mathbf{q}^{ext,e,\alpha} = \int_V \begin{Bmatrix} M_1\mathbf{P}_{\mathrm{V}} \\ M_2\mathbf{P}_{\mathrm{V}} \\ M_3\mathbf{P}_{\mathrm{V}} \end{Bmatrix} dV + \int_{Sp} \begin{Bmatrix} M_1\mathbf{P}_{\mathrm{S}} \\ M_2\mathbf{P}_{\mathrm{S}} \\ M_3\mathbf{P}_{\mathrm{S}} \end{Bmatrix} dS. \tag{24}$$

Thus, the present numerical model is described by a set of non-linear equations defined as functions of three independent variables $\mathbf{u}$, $\mathbf{Q}$ and $\boldsymbol{\alpha}$. A lengthy, but otherwise straight-forward method for solving this system of non-linear equations would be to linearize the whole system and solve it as a sequence of linear equations for all independent variables. However, since the incompatible-mode parameters are defined only element-wise, i.e. they are not shared between elements, a static condensation approach is possible, which significantly reduces the number of equations we need to solve. The static condensation is part of a so-called operator split solution method, consisting of expressing the incompatible mode parameter $\boldsymbol{\alpha}^e$ as a function of the remaining variables. After that, linearisation of the residual vectors is performed, which allows us to solve the system of nonlinear equations as a sequence of linear problems.

3.1. Incompatible-mode residual $\mathbf{g}^{e,\alpha}$ at the element level

In order to obtain the incompatible-mode parameter $\boldsymbol{\alpha}^e$ we note that the incompatible-mode residual at the element level

$$\mathbf{g}^{e,\alpha} = \int_V \begin{Bmatrix} \mathbf{QB}(M_1\nabla_X) \\ \mathbf{QB}(M_2\nabla_X) \\ \mathbf{QB}(M_3\nabla_X) \end{Bmatrix} dV - \mathbf{q}^{ext,e,\alpha}, \tag{25}$$

must be equal to zero for a particular value of $\mathbf{u}^e$, $\mathbf{Q}^e$ and $\boldsymbol{\alpha}^e$. Here we analyse the incompatible-mode residual equation where we aim to express the incompatible-mode parameter $\boldsymbol{\alpha}^e$ explicitly. In order to do that, important equalities defined in [21] outlined below are used and introduced into equation (25).

By introducing expression (9) into the element incompatible-mode residual (25) and by applying tensor identities defined in Appendix B of [18] we obtain:

$$\begin{aligned} &\mathbf{QB}(M_a\nabla_X) \\ &\quad = \mathbf{Q}\left(\mathbf{T} : \mathbf{E}\right)(M_a\nabla_X) \\ &\quad = \lambda\mathbf{Q}\left(M_a\nabla_X\right)\mathrm{tr}(\mathbf{E}) + (\mu+\nu)\mathbf{QE}\left(M_a\nabla_X\right) + (\mu-\nu)\mathbf{QE}^{\mathrm{T}}\left(M_a\nabla_X\right). \end{aligned} \tag{26}$$

Now we can rewrite the incompatible-mode residual vector (25) using (26) as

$$\begin{aligned} \mathbf{g}^{e,\alpha} = \int_V \begin{Bmatrix} \lambda\mathbf{Q}\left(M_1\nabla_X\right)\mathrm{tr}(\mathbf{E}) + (\mu+\nu)\mathbf{QE}\left(M_1\nabla_X\right) + (\mu-\nu)\mathbf{QE}^{\mathrm{T}}\left(M_1\nabla_X\right) \\ \lambda\mathbf{Q}\left(M_2\nabla_X\right)\mathrm{tr}(\mathbf{E}) + (\mu+\nu)\mathbf{QE}\left(M_2\nabla_X\right) + (\mu-\nu)\mathbf{QE}^{\mathrm{T}}\left(M_2\nabla_X\right) \\ \lambda\mathbf{Q}\left(M_3\nabla_X\right)\mathrm{tr}(\mathbf{E}) + (\mu+\nu)\mathbf{QE}\left(M_3\nabla_X\right) + (\mu-\nu)\mathbf{QE}^{\mathrm{T}}\left(M_3\nabla_X\right) \end{Bmatrix} dV \\ - \mathbf{q}^{ext,e,\alpha} = \mathbf{0}. \end{aligned} \tag{27}$$

Next, by introducing the interpolation of the displacement field as

$$\mathbf{u}^h = \sum_{i=1}^{8} N_i(\xi,\eta,\zeta)\mathbf{u}_i^e + \sum_{b=1}^{3} M_b(\xi,\eta,\zeta)\boldsymbol{\alpha}_b^e. \tag{28}$$

into the Biot-like strain tensor, and the obtained result in equation (26) we get

$$\mathbf{QB}(M_a\nabla_X) \tag{29}$$

$$\begin{aligned}
&= \lambda\mathbf{Q}\left(M_a\nabla_X\right)\nabla_X^{\mathrm{T}}\mathbf{Q}^{\mathrm{T}}\left(\sum_{i=1}^{8}N_i(\xi,\eta,\zeta)\mathbf{u}_i^e+\sum_{b=1}^{3}M_b(\xi,\eta,\zeta)\boldsymbol{\alpha}_b^e\right)\\
&+\lambda\mathbf{Q}\left(M_a\nabla_X\right)\mathrm{tr}\left(\mathbf{Q}^{\mathrm{T}}\right)-3\lambda\mathbf{Q}\left(M_a\nabla_X\right)\\
&+(\mu+\nu)\left(\nabla_X^{\mathrm{T}}M_a\nabla_X\right)\left(\sum_{i=1}^{8}N_i(\xi,\eta,\zeta)\mathbf{u}_i^e+\sum_{b=1}^{3}M_b(\xi,\eta,\zeta)\boldsymbol{\alpha}_b^e\right)\\
&+(\mu+\nu)\mathbf{I}(M_a\nabla_X)-(\mu+\nu)\mathbf{Q}(M_a\nabla_X)\\
&+(\mu-\nu)\mathbf{Q}\nabla_X(M_a\nabla_X^{\mathrm{T}})\mathbf{Q}^{\mathrm{T}}\left(\sum_{i=1}^{8}N_i(\xi,\eta,\zeta)\mathbf{u}_i^e+\sum_{b=1}^{3}M_b(\xi,\eta,\zeta)\boldsymbol{\alpha}_b^e\right)\\
&+(\mu-\nu)\mathbf{QQ}(M_a\nabla_X)-(\mu-\nu)\mathbf{Q}(M_a\nabla_X)
\end{aligned} \tag{30}$$

The detailed derivation procedure is given in Appendix A. Next, we substitute equation (30) in the element residual vector (27), and, by grouping terms multiplying the same variables, obtain new matrices multiplying the element nodal displacements and the incompatible-mode parameters giving the following final form of the incompatible-mode residual vector:

$$\tilde{\mathbf{F}}^e\mathbf{u}^e+\mathbf{H}^e\boldsymbol{\alpha}^e=\mathbf{r}^{\alpha,e}+\mathbf{q}^{ext,e,\alpha}, \tag{31}$$

where the matrices $\tilde{\mathbf{F}}^e$ and $\mathbf{H}^e$ and the vector $\mathbf{r}^{\alpha,e}$ are independent of $\mathbf{u}^e$ and $\boldsymbol{\alpha}^e$. Thus, we can see that equation (31) is linear considering the incompatible-mode parameter $\boldsymbol{\alpha}^e$ which allows us to express it as

$$\boldsymbol{\alpha}^e=\mathbf{H}^{e^{-1}}\left(\mathbf{r}^{\alpha,e}+\mathbf{q}^{ext,e,\alpha}-\tilde{\mathbf{F}}^e\mathbf{u}^e\right). \tag{32}$$

The form of matrices $\tilde{\mathbf{F}}^e$ and $\mathbf{H}^e$ and the form of the vector $\mathbf{r}^{\alpha,e}$ are obtained as given next.

3.1.1. Matrix $\tilde{\mathbf{F}}^e$

The block matrix $\tilde{\mathbf{F}}_{aj}$ is equal to

$$\tilde{\mathbf{F}}_{aj}=\lambda\mathbf{Q}(M_a\nabla_X)(N_j\nabla_X)^{\mathrm{T}}\mathbf{Q}^{\mathrm{T}}+(\mu+\nu)(N_j\nabla_X)^{\mathrm{T}}(M_a\nabla_X)\mathbf{I}+(\mu-\nu)\mathbf{Q}(N_j\nabla_X)(M_a\nabla_X)^{\mathrm{T}}\mathbf{Q}^{\mathrm{T}}, \tag{33}$$

giving the $[9 \times 24]$ element matrix as

$$\tilde{\mathbf{F}}^e = \int_V \begin{bmatrix} \tilde{\mathbf{F}}_{11} & \tilde{\mathbf{F}}_{12} & \tilde{\mathbf{F}}_{13} & \tilde{\mathbf{F}}_{14} & \tilde{\mathbf{F}}_{15} & \tilde{\mathbf{F}}_{16} & \tilde{\mathbf{F}}_{17} & \tilde{\mathbf{F}}_{18} \\ \tilde{\mathbf{F}}_{21} & \tilde{\mathbf{F}}_{22} & \tilde{\mathbf{F}}_{23} & \tilde{\mathbf{F}}_{24} & \tilde{\mathbf{F}}_{25} & \tilde{\mathbf{F}}_{26} & \tilde{\mathbf{F}}_{27} & \tilde{\mathbf{F}}_{28} \\ \tilde{\mathbf{F}}_{31} & \tilde{\mathbf{F}}_{32} & \tilde{\mathbf{F}}_{33} & \tilde{\mathbf{F}}_{34} & \tilde{\mathbf{F}}_{35} & \tilde{\mathbf{F}}_{36} & \tilde{\mathbf{F}}_{37} & \tilde{\mathbf{F}}_{38} \end{bmatrix} dV. \tag{34}$$

3.1.2. Matrix $\mathbf{H}^e$

The block matrix $\mathbf{H}_{ab}$ is equal to

$$\mathbf{H}_{ab} = \lambda \mathbf{Q}(M_a \nabla_X)(M_b \nabla_X)^{\mathrm{T}} \mathbf{Q}^{\mathrm{T}} + (\mu+\nu)(M_b \nabla_X)^{\mathrm{T}}(M_a \nabla_X)\mathbf{I} + (\mu-\nu)\mathbf{Q}(M_b \nabla_X)(M_a \nabla_X)^{\mathrm{T}} \mathbf{Q}^{\mathrm{T}}, \tag{35}$$

giving the $[9 \times 9]$ element matrix:

$$\mathbf{H}^e = \int_V \begin{bmatrix} \mathbf{H}_{11} & \mathbf{H}_{12} & \mathbf{H}_{13} \\ \mathbf{H}_{21} & \mathbf{H}_{22} & \mathbf{H}_{23} \\ \mathbf{H}_{31} & \mathbf{H}_{32} & \mathbf{H}_{33} \end{bmatrix} dV. \tag{36}$$

3.1.3. Vector $\mathbf{r}^{\alpha,e}$

The block vector $\mathbf{r}_a^\alpha$ is equal to

$$\begin{aligned} \mathbf{r}_a^\alpha = &-\lambda \mathbf{Q} \left(M_a \nabla_X\right) \mathrm{tr}\left(\mathbf{Q}^{\mathrm{T}}\right) + 3\lambda \mathbf{Q} \left(M_a \nabla_X\right) - (\mu-\nu)\mathbf{Q}\mathbf{Q}(M_a \nabla_X) + (\mu-\nu)\mathbf{Q}(M_a \nabla_X) \\ &- (\mu+\nu)\mathbf{I}(M_a \nabla_X) + (\mu+\nu)\mathbf{Q}(M_a \nabla_X), \end{aligned} \tag{37}$$

giving the $[9 \times 1]$ element vector

$$\mathbf{r}^\alpha = \begin{Bmatrix} \mathbf{r}_1^\alpha \\ \mathbf{r}_2^\alpha \\ \mathbf{r}_3^\alpha \end{Bmatrix}. \tag{38}$$

Even thought it is observed that this problem is linear considering the incompatible-mode parameters, it is still highly non-linear regarding the displacements and rotations.

3.2. Linearisation of the residual force vector $\mathbf{g}^e$ *and the incompatible-mode residual* $\mathbf{g}^{e,\alpha}$

The solution of this nonlinear problem can be obtained by the Newton-Raphson iterative solution procedure, for which the residual vectors have to be linearised, as follows:

$$\mathrm{Lin}\left\{\begin{array}{c}\mathbf{g}\\ \mathbf{g}^{\alpha}\end{array}\right\}=\left\{\begin{array}{c}\mathbf{g}\\ \mathbf{g}^{\alpha}\end{array}\right\}+\left\{\begin{array}{c}\Delta\mathbf{g}\\ \Delta\mathbf{g}^{\alpha}\end{array}\right\}=\mathbf{0}, \tag{39}$$

which written on the element level reads

$$\mathrm{Lin}\left\{\begin{array}{c}\mathbf{g}^{e}\\ \mathbf{g}^{e,\alpha}\end{array}\right\}=\left\{\begin{array}{c}\mathbf{g}^{e}\\ \mathbf{g}^{e,\alpha}\end{array}\right\}+\left\{\begin{array}{c}\Delta\mathbf{g}^{e}\\ \Delta\mathbf{g}^{e,\alpha}\end{array}\right\}. \tag{40}$$

If we separate these equations we will obtain the following general structure:

$$\mathrm{Lin}[\mathbf{g}^{e}]=\mathbf{g}^{e}+\Delta\mathbf{g}^{e}=\mathbf{q}^{int,e}-\mathbf{q}^{ext,e}+\mathbf{K}^{e}\Delta\mathbf{d}^{e}+\mathbf{F}^{e^{\mathrm{T}}}\Delta\boldsymbol{\alpha}^{e}=\mathbf{0}, \tag{41}$$

$$\mathrm{Lin}[\mathbf{g}^{e,\alpha}]=\mathbf{g}^{e,\alpha}+\Delta\mathbf{g}^{e,\alpha}=\mathbf{g}^{e,\alpha}+\mathbf{F}^{e}\Delta\mathbf{d}^{e}+\mathbf{H}^{e}\Delta\boldsymbol{\alpha}^{e}=\mathbf{0}, \tag{42}$$

which can be written in the matrix form as

$$\begin{bmatrix}\mathbf{K}^{e} & \mathbf{F}^{e^{\mathrm{T}}}\\ \mathbf{F}^{e} & \mathbf{H}^{e}\end{bmatrix}\left\{\begin{array}{c}\Delta\mathbf{d}^{e}\\ \Delta\boldsymbol{\alpha}^{e}\end{array}\right\}=\left\{\begin{array}{c}\mathbf{q}^{ext,e}-\mathbf{q}^{int,e}\\ -\mathbf{g}^{e,\alpha}\end{array}\right\}, \tag{43}$$

where $\mathbf{K}^{e}$ represents the element tangent stiffness matrix obtained by using the conventional Lagrange interpolation, as presented in [21] and [18]. However, since we required the incompatible-mode residual to be zero for a chosen value of $\mathbf{u}^{e}$, $\mathbf{Q}^{e}$ and $\boldsymbol{\alpha}^{e}$, i.e. $\mathbf{g}^{e,\alpha}(\mathbf{u}^{e},\mathbf{Q}^{e},\boldsymbol{\alpha}^{e})=\mathbf{0}$, the previous system of equations is reduced to

$$\begin{bmatrix}\mathbf{K}^{e} & \mathbf{F}^{e^{\mathrm{T}}}\\ \mathbf{F}^{e} & \mathbf{H}^{e}\end{bmatrix}\left\{\begin{array}{c}\Delta\mathbf{d}^{e}\\ \Delta\boldsymbol{\alpha}^{e}\end{array}\right\}=\left\{\begin{array}{c}\mathbf{q}^{ext,e}-\mathbf{q}^{int,e}\\ \mathbf{0}\end{array}\right\}. \tag{44}$$

Element matrices $\mathbf{K}^{e}$ and $\mathbf{F}^{e}$ from equation (43) are described in detail in Appendix B, while matrix $\mathbf{H}^{e}$ is equal to the one obtained for the zero incompatible-mode residual and is defined in Section 3.1.2.

In order to eliminate the presence of the unknown incompatible-mode parameter increment $\Delta\boldsymbol{\alpha}^{e}$ we perform the so-called static condensation at the element level by expressing $\Delta\boldsymbol{\alpha}^{e}$ from the second equation (44_2) as

$$\Delta\boldsymbol{\alpha}^{e}=-\mathbf{H}^{e^{-1}}\mathbf{F}^{e}\Delta\mathbf{d}^{e} \tag{45}$$

and substitute it in the first equation (44_1) which gives a reduced (condensed) stiffness matrix

$$\tilde{\mathbf{K}}^e = \mathbf{K}^e - \mathbf{F}^{e^{\mathrm{T}}} \mathbf{H}^{e^{-1}} \mathbf{F}^e. \tag{46}$$

From this point on we follow the standard finite element assembly procedure. For clearer understanding, the step-by-step algorithm implementation together with the iterative update procedure is given in Appendix C.

4. Numerical examples

The newly presented enhanced finite element which we will refer to as Hex8NLIM is implemented in The Finite Element Analysis Programme FEAP [25]. The implemented finite element is thus tested against a non-linear micropolar analytical solution available in the literature [26] on a pure-bending problem of a cantilever beam. Precision and robustness of the element is tested for high-curvature deformation states and a parameter sensitivity analysis has been performed. The finite-element performance is then compared against the geometrically non-linear hexahedral Lagrangian finite elements of first and second order presented in [18], which we refer to as Hex8NL and Hex27NL. A genuine 3D deformation is considered on a cantilever beam curved in plane with an out-of-plane loading and the obtained results are compared against a solution in classical elasticity and the numerical results from [18].

4.1. Pure bending problem of a cantilever beam

The pure-bending state of a beam is a state in which the beam is bent into a circular shape with the beam cross-sections planar and perpendicular to the axis of the beam. The micropolar analytical solution of this problem in the linear regime is given by Gauthier and Jahsman [8], where it is shown that the resultant bending moment has to be applied as a combination of a linearly varying longitudinal load and a constant moment load in an exactly defined proportion, in order to obtain a pure bending state [27]. Furthermore, it is observed that the characteristic bending length is the material parameter responsible for stiffer response of the structure analysed, representing the microstructural effect. In

order to test finite elements in the geometrically nonlinear regime, an analytical solution of the pure bending problem in the geometrically nonlinear micropolar elasticity has been provided in [18], representing a micropolar generalisation of the Euler-elastica solution. However, it is observed that the solution given in [18] is valid only for thin specimens, where through-the-thickness stresses and strains do not significantly develop. In what follows we will refer to solution [18] as the *approximate analytical solution*. A closed-form analytical solution of the pure bending problem is given in [26], where in addition to the stiffening effect due to the microstructure of the material, the softening effect due to nonlinearity is present, which is not recognised in the approximate solution [18]. We refer to the solution [26] as the *exact analytical solution*.

4.1.1. Thin cantilever beam [18]

First we choose to test the new finite element on the example described in [18] for which we know that the difference between the two available analytical solutions is negligible. We model a thin cantilever beam subject to end loading resulting in a pure moment, shown in Figure 2. The dimensions of the cantilever are $L = 10$ m, $h = 0.1$ m and $b = 1$ m, and, in order to capture the size-effect the value of the characteristic bending length is varied as $l_b \in \{0.01, 0.02, 0.04, 0.08\}$ m. The resultant bending moment chosen as $M_z = 0.01\pi$ Nm is applied through a linearly varying surface loading P_{S1} and a constant surface moment loading M_{S3} in the proportion defined in equations (16) and (17) from [26], which has to be strictly respected in order to obtain a pure bending state. In addition, the surface loading P_{S1} has to be applied as a follower load, i.e. it has to remain orthogonal to the cantilever cross-section during the whole deformation process.

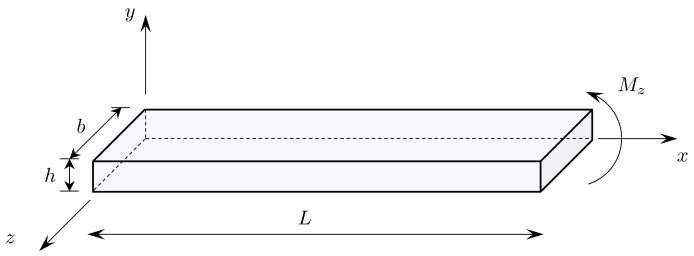

Figure 2: Thin cantilever beam subject to bending

The engineering material parameters are taken as $E = 1200$ N/m^2 and $n = 0.0$ which give the Lamé constants $\mu = 600$ N/m^2 and $\lambda = 0$ N/m^2. The parameter ν is chosen to be equal to $\nu = 200$ N/m^2, corresponding to $N = 0.5$, but in this example it can have an arbitrary value since it does not affect the solution. The engineering parameters which exist only in the 3D analysis are chosen as $\psi = 1$ and $l_t = 0.02$ m, but, since they also do not affect the solution, they can also have arbitrary values, giving $\alpha = 0$ N and $\beta = 0.24$ N. The chosen value of the characteristic bending length give $\gamma \in \{0.0, 0.72, 3.6, 15.12\}$ N. Along the left-hand edge of the specimen the following displacements and microrotations are restrained $u_1(0, y, z) = u_3(0, y, z) = \varphi_1(0, y, z) = \varphi_2(0, y, z) = \varphi_3(0, y, z) = 0$, for $y \in [0, h]$ and $z \in [0, b]$, while the vertical displacement is restrained only on the bottom, i.e. $u_2(0, 0, z) = 0$ for $z \in [0, b]$. Furthermore, the cylindrical bending is accomplished by additionally restraining the displacements in the z direction along the whole cantilever, i.e. $u_3(x, y, z) = 0$ for $x \in [0, L]$, $y \in [0, h]$ and $z \in [0, b]$. The obtained numerical results are presented in Tables 1, 2 and 3 for Hex8NL, Hex8NLIM and Hex27NL, respectively, for a mesh of 16 finite elements propagating in the longitudinal direction. The relative error obtained in the kinematic fields is expressed as $\varepsilon = |\frac{u_N - u_A}{u_N}| \cdot 100\%$ where subscripts N and A are referred to numerical and analytical solutions. It can be observed that the first order Lagrangian element gives very poor results for such a coarse mesh. The newly presented Hex8NLIM element and the Lagrangian element of second order almost reproduce the analytical result for such a coarse mesh,

with a slightly higher accuracy of the enhanced Hex8NLIM element. However, the computational time needed for the Hex8NLIM element to converge is more than 25 times lower than for the Hex27NL element, which makes it significanlly more efficient. By increasing the finite element mesh the analytical result is approached in all fields for all three elements.

Table 1: Results in node $P = (10.0, 0.1, 1.0)$ obtained using $16 \times 1 \times 1$ Hex8NL elements, A = Analytical, N = Numerical, LS = Number of load steps, ε = error

l_b	LS	u_1			u_2			φ_3			niter	CPU
		A	N	ε [%]	A	N	ε [%]	A	N	ε [%]		time
0.01	1	-7.774	-0.028	99.67	7.096	0.575	91.90	2.534	0.115	95.46	5	0.16 sec
0.02	1	-3.814	-0.027	99.29	6.387	0.560	91.23	1.603	0.112	93.01	5	0.17 sec
0.04	1	-0.718	-0.022	96.94	3.123	0.508	83.74	0.649	0.102	84.28	5	0.15 sec
0.08	1	-0.071	-0.013	81.69	0.956	0.370	61.30	0.192	0.074	61.46	5	0.14 sec

Table 2: Results in node $P = (10.0, 0.1, 1.0)$ obtained using $16 \times 1 \times 1$ Hex8NLIM elements, A = Analytical, N = Numerical, LS = Number of load steps, ε = error

l_b	LS	u_1			u_2			φ_3			niter	CPU
		A	N	ε [%]	A	N	ε [%]	A	N	ε [%]		time
0.01	4	-7.774	-7.636	1.78	7.096	7.112	0.22	2.534	2.505	1.14	13,13,13,11	1.30 sec
0.02	2	-3.814	-3.797	0.45	6.387	6.377	0.16	1.603	1.599	0.25	15,16	0.82 sec
0.04	1	-0.718	-0.718	0.00	3.123	3.123	0.00	0.649	0.649	0.00	11	0.32 sec
0.08	1	-0.071	-0.071	0.00	0.956	0.956	0.00	0.192	0.192	0.00	6	0.20 sec

Table 3: Results in node $P = (10.0, 0.1, 1.0)$ obtained using $16 \times 1 \times 1$ Hex27NL elements, A = Analytical, N = Numerical, LS = Number of load steps, ε = error

l_b	LS	u_1			u_2			φ_3			niter	CPU
		A	N	ε [%]	A	N	ε [%]	A	N	ε [%]		time
0.01	4	-7.774	-7.520	3.27	7.096	7.128	0.45	2.534	2.472	2.45	13,13,11,11	33 sec
0.02	2	-3.814	-3.772	1.10	6.387	6.364	0.36	1.603	1.592	0.67	13,15	18 sec
0.04	1	-0.718	-0.717	0.14	3.123	3.122	0.03	0.649	0.649	0.00	11	8 sec
0.08	1	-0.071	-0.071	0.00	0.956	0.956	0.00	0.192	0.192	0.00	6	5 sec

4.1.2. High curvature deformation of the cantilever beam

Next we want to test the performance of the numerical solution for high curvature deformation states for various length-to-height ratio of the cantilever beam. The length and width of the beam are kept fixed, i.e. $L = 10$ m and $b = 1$ m and the height of the beam is varied as $h \in \{0.1, 1, 2, 4\}$ m. If not stated differently, the material parameters are taken as: $E = 1200$ N/m^2 and $n = 0.0$ which give the Lamé constants $\mu = 600$ N/m^2 and $\lambda = 0$ N/m^2. The parameter ν is chosen to be equal to $\nu = 200$ N/m^2, corresponding to $N = 0.5$ and the polar ratio is chosen as $\psi = 1$, giving $\alpha = 0$ N. The characteristic bending and torsion length are chosen in proportion to the height of the beam as $l_b = 0.3h$ and $l_t = 0.1h$. The resultant bending moment is chosen so as to produce for each h the deformed shape of a nearly closed circular ring. Furthermore, in order to better understand the difference between the approximate analytical solution [18] and the exact analytical solution [26], for each case analysed, the analytical deformation state, together with the analytical displacements and microrotation is given. Also, the external bending moment M_z, is applied as a combination of a linearly varying surface loading of a magnitude p_0 at the edges of the cross-section and a constant moment surface loading of magnitude m_0. According to the approximate solution their values are obtained as: $p_0 = \frac{1}{1+\delta}\frac{M_z}{W_z}$ and $m_0 = \frac{\delta}{1+\delta}\frac{M_z}{A}$ with $A = bh$, $W_z = \frac{bh^2}{6}$ and $\delta = 24(l_b/h)^2$. Regarding the exact analytical solution, their values are expressed in terms of hyperbolic functions

and can be found in [26], equations (16) and (17). For more details see [26]. The obtained values are outlined with respect to the chosen analytical solution for each case analysed.

CASE 1: $h = 0.1\ m$

In case 1 we analyse a cantilever beam with a length-to-height ratio $\frac{L}{h} = 100$. The resultant bending moment is chosen to be equal to $M_z = 0.1902\ Nm$, which, according to both analytical solutions produces the radius of curvature of the unstrained longitudinal fibres $\rho = 1.66\ m$. From Table 4 and Figure 3 we can see that the approximate solution coincides with the exact analytical solution for the number of significant digits shown. The problem is solved with a mesh of 64 finite elements propagating in the longitudinal direction (Hex8NL, Hex8NLIM, Hex27NL elements). The obtained results are presented in Table 5 and Figure 4. It can be observed that Hex8NLIM and Hex27NL reproduce the analytical solution, but with more than 62 times lower computational time needed for the enhanced element. Hex8NL, however, is very far from the analytical solution for the chosen mesh and finite element aspect ratio, due to the presence of a shear locking effect. By refining the finite element mesh, the shear locking effect vanishes and the analytical solution is approached in all fields. Since the mesh of 64 finite elements was dense enough to reproduce the analytical solution in 2 significant digits for the Hex8NLIM and Hex27NL elements, we keep this mesh for the next cases analysed.

Table 4: CASE 1: Comparison of the analytical solutions for $L = 10\ m$, $h = 0.1\ m$, $E = 1200$ N/m^2, $n = 0.0$, $l_b = 0.03$ m, for a high curvature deformation state. Results are obtained at node $P = (L, h, b)$

	Exact solution [26]						Approximate solution [18]					
M_z [Nm]	m_0	p_0	ρ [m]	φ_z	u_1 [m]	u_2 [m]	m_0	p_0	ρ [m]	φ_z	u_1 [m]	u_2 [m]
0.1902	1.30	36.10	1.66	6.02	-10.42	0.06	1.30	36.10	1.66	6.02	-10.42	0.06

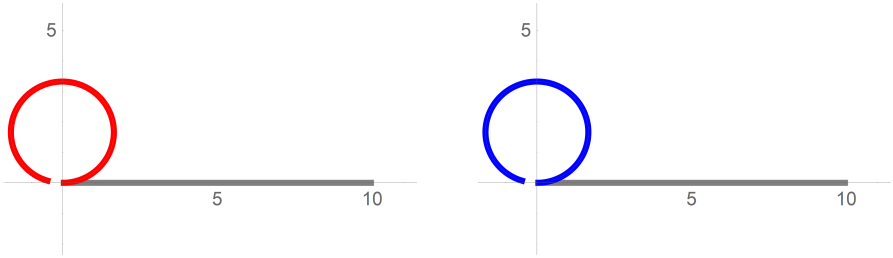

(a) Exact solution [26] (b) Approximate solution [18]

Figure 3: Pure bending of a thin cantilever beam (case 1)

Table 5: Case 1: Numerical results in node $P = (L, h, b)$, LS - Number of load steps, ε - error

El	Nel	LS	u_1	ε [%]	u_2	ε [%]	φ_3	ε [%]	CPU time
Hex8NL	64	10	-11.82	13.43	4.13	6783.33	3.97	34.05	8 sec
Hex8NLIM	64	10	-10.42	0.00	0.06	0.00	6.02	0.00	11 sec
Hex27NL	64	10	-10.42	0.00	0.06	0.00	6.02	0.00	8 min 19 sec

(a) Hex8NL (b) Hex8NLIM (c) Hex27NL

Figure 4: Numerical solution for case 1 using 64 elements

335 ***CASE 2:*** $h = 1.0\ m$

In case 2 we analyse the cantilever beam with a length-to-height ratio $\frac{L}{h} = 10$. The resultant bending moment is chosen to be equal to $M_z = 186.05\ Nm$, which, according to both analytical solutions produces a radius of curvature

of the unstrained longitudinal fibres $\rho = 1.66\ m$. From Table 6 and Figure 5 we can see that in this case the approximate solution starts to differ from the exact analytical solution, predicting a stiffer response of the beam. However, the difference is still not significant. The problem is solved with a mesh of 64 finite elements propagating in the longitudinal direction with Hex8NL, Hex8NLIM, Hex27NL elements. The obtained results are presented in Table 7. Again, Hex8NLIM and Hex27NL give numerical results which are very close to the analytical solution, with a 54 times lower cost of the Hex8NLIM element. Hex8NL shows much better performance than in case 1.

Table 6: Case 2: Comparison of the analytical solutions for $L = 10\ m$, $h = 1\ m$, $E = 1200\ \mathrm{N/m^2}$, $n = 0.0$, $l_b = 0.3$ m, for a high curvature deformation. Results are obtained at node $P = (L, h, b)$

	Exact solution [26]						Approximate solution [18]					
M_z [Nm]	m_0 [Nm]	p_0	ρ [m]	φ_z	u_1 [m]	u_2 [m]	m_0	p_0	ρ [m]	φ_z	u_1 [m]	u_2 [m]
186.05	130.0	350.592	1.66	6.02	-10.31	0.03	127.18	353.27	1.66	5.90	-10.46	0.09

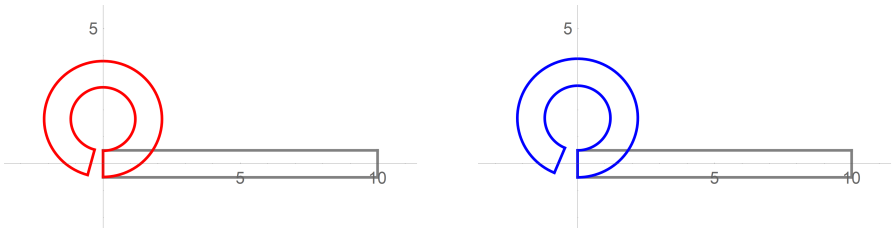

(a) Exact solution [26]

(b) Approximate solution [18]

Figure 5: Pure bending of a cantilever beam (case 2)

Table 7: Case 2: Numerical results at node $P = (L, h, b)$, LS - Number of load steps, ε - error

El	Nel	LS	u_1	ε [%]	u_2	ε [%]	φ_3	ε [%]	CPU time
Hex8NL	64	150	-10.63	3.10	0.09	200.00	5.99	0.50	1 min 8 sec
Hex8NLIM	64	150	-10.56	2.42	0.07	133.33	6.02	0.00	1 min 20 sec
Hex27NL	64	150	-10.56	2.42	0.07	133.33	6.02	0.00	54 min 10 sec

CASE 3: $h = 2.0\ m$

In case 3 we further decrease the cantilever beam length-to-height ratio to $\frac{L}{h} = 5$. The resultant bending moment is chosen to be equal to $M_z = 1419.31\ Nm$, which, according to the analytical solution produces a radius of curvature of the longitudinally unstrained fibre $\rho = 1.65\ m$. From Table 8 and Figure 6 we can see that the approximate solution now differs more from the exact analytical solution, predicting an 8% higher radius of curvature. The problem is again solved with a mesh of 64 finite elements propagating in the longitudinal direction with Hex8NL, Hex8NLIM, Hex27NL elements. The obtained results are presented in Table 9. In case 3, all the elements give a numerical solution which is in good agreement with the exact analytical solution, with a high efficiency of the Hex8NL and Hex8NLIM elements. However, as already observed, Hex27NL is shown to be computationally very expensive.

Table 8: Case 3: Comparison of the analytical solutions for $L = 10\ m$, $h = 2\ m$, $E = 1200$ N/m^2, $n = 0.0$, $l_b = 0.6$ m for a high curvature deformation. Results are obtained at node $P = (L, h, b)$

	Exact solution [26]						Approximate solution [18]					
M_z [Nm]	m_0	p_0	ρ [m]	φ_z	u_1 [m]	u_2 [m]	m_0	p_0	ρ [m]	φ_z	u_1 [m]	u_2 [m]
1419.31	525.0	650.96	1.65	6.08	-10.16	-0.09	485.08	673.72	1.78	5.61	-10.48	0.17

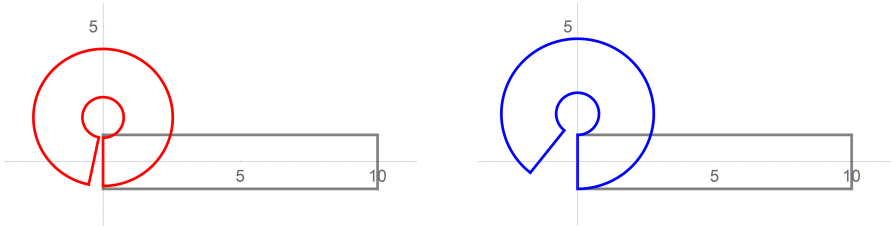

(a) Exact solution [26] (b) Approximate solution [18]

Figure 6: Pure bending of a cantilever beam (case 3)

Table 9: Case 3: Numerical results at node $P = (L, h, b)$, LS - Number of load steps, ε - error

El	Nel	LS	u_1	ε [%]	u_2	ε [%]	φ_3	ε [%]	CPU time
Hex8NL	64	150	-10.53	3.64	0.06	166.67	6.07	0.17	1 min 7 sec
Hex8NLIM	64	150	-10.51	3.44	0.05	155.56	6.08	0.00	1 min 23 sec
Hex27NL	64	150	-10.51	3.44	0.05	155.56	6.08	0.00	58 min 48 sec

CASE 4: $h = 4.0\ m$

Finally, in case 4 we further increase the beam height to obtain a length-to-height ratio $\frac{L}{h} = 2.5$. The resultant bending moment is chosen to be equal to $M_z = 9581.59\ Nm$, which, according to the exact analytical solution produces a radius of curvature of the longitudinally unstrained fiber $\rho = 1.73\ m$. From Table 10 and Figure 7 we can see that here the approximate solution differs significanlty from the exact analytical solution. In this thick-cantilever beam example, we can clearly see from Figure 10 that through-the-thickness strains develop even for a zero Poisson's ratio material, leading to a shrinkage in the beam height. Furthermore, due to the lack of the non-linear softening effect [26] in the approximate solution, a stiffer response is predicted, producing a deformation state with 22% higher radius of curvature. These two effects come to the fore for thick beams. The problem is solved with a mesh of 64 finite

elements propagating in the longitudinal direction with Hex8NL, Hex8NLIM, Hex27NL elements, first for the value of the coupling number $N = 0.5$. It is observed that none of the finite elements converge to a numerical solution in the Newton-Raphson process for the chosen values of material parameters for different mesh densities and load increments. Thus, a test has been made to check weather the values of certain material parameters which do not exist in the analytical solution affect the convergence of the numerical solution. It is observed that by increasing the value of the coupling number $N = 0.9$ a numerical convergence is achieved. The obtained results are presented in Table 11 from where we can see that a good agreement between the analytical and numerical solution is obtained. This observation motivated us to perform an extensive parameter identification analysis presented in the next section.

Table 10: Case 4: Comparison of the analytical solutions for $L = 10\ m$, $h = 4\ m$, $E = 1200\ \mathrm{N/m^2}$, $n = 0.0$, $l_b = 1.2$ m for a high curvature deformation. Results are obtained at node $P = (L, h, b)$

	Exact solution [26]						Approximate solution [18]					
M_z [Nm]	m_0	p_0	ρ [m]	φ_z	u_1 [m]	u_2 [m]	m_0	p_0	ρ [m]	φ_z	u_1 [m]	u_2 [m]
9581.59	2000.0	984.23	1.73	5.79	-10.15	-0.55	1637.36	1137.06	2.11	4.74	-10.11	0.11

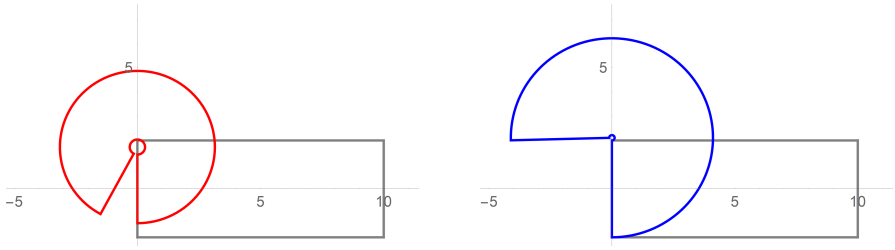

(a) Exact solution [26]

(b) Approximate solution [18]

Figure 7: Pure bending of a thick cantilever beam (case 4)

Table 11: Case 4: Numerical results at node $P = (L, h, b)$, LS - Number of load steps, ε - error

El	Nel	LS	u_1	ε [%]	u_2	ε [%]	φ_3	ε [%]	CPU time
Hex8NL	64	220	-11.41	2.56	0.34	161.82	5.80	0.17	1 min 28 sec
Hex8NLIM	64	220	-11.38	2.26	0.32	158.18	5.81	0.34	1 min 45 sec
Hex27NL	64	220	-11.38	2.26	0.33	160.00	5.82	0.51	70 min 37 sec

4.1.3. Parameter sensitivity analysis

In order to check the numerical solution sensitivity to the choice of micropolar material parameters which are not present in the analytical solution, a new setup is analysed with the following geometry: $L = 10\ m$, $h = 1\ m$, $b = 1\ m$, and the following material parameters are kept fixed $E = 1200\ \mathrm{N/m^2}$, $n = 0.0$, $l_b = 0.15$ m, $l_t = 0.04$ m giving the analytical solution from Table 12 and Figure 8.

Table 12: Analytical solution for $L = 10\ m$, $h = 1\ m$, $E = 1200\ \mathrm{N/m^2}$, $n = 0.0$, $l_b = 0.15$

	Exact solution [26]					
M_z	m_0	p_0	ρ	φ_z	u_1	u_2
90.85	33.43	360.0	1.61	6.19	-10.11	0.01

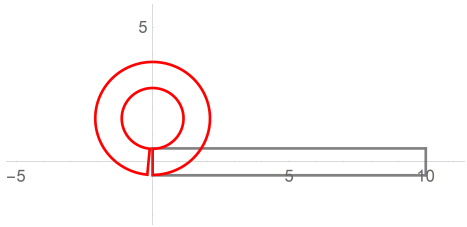

Figure 8: Exact solution [26] for pure bending of a cantilever beam

First we test the problem by keeping the polar ratio fixed and equal to $\psi = 1$, and we vary the value of the coupling number $N \in \{0.1, 0.5, 0.9\}$. From Table 13 it can be observed that the value of the coupling number affects the solution in both precision and robustness. For $N = 0.1$ none of the elements converge to a numerical solution. Element Hex8NL converges to a numerical solution for $N = 0.5$ and $N = 0.9$. However, it can be observed that for a higher value of the coupling number the obtained numerical solution is farther from the analytical solution than that obtained with lower value of the coupling number. The second order element Hex27NL fails to converge to a numerical solution for all chosen values of the coupling number. The enhanced Hex8NLIM element converges to a numerical solution for $N = 0.5$ and $N = 0.9$ and the obtained solution is in good agreement with the analytical solution for the horizontal displacement and microrotation for both chosen values (Table 13). Regarding the vertical displacement, a further refinement of the finite element mesh in the transversal direction would be needed in order to obtain more accurate values.

Table 13: Variation of the coupling number $N \in \{0.1, 0.5, 0.9\}$ for $E = 1200$ N/m^2, $n = 0.0$, $l_b = 0.15$ m, $l_t = 0.04$ m, $\psi = 1.0$: Results at node $P = (L, h, b)$, A = Analytical, N = Numerical, LS = Number of load steps, NC = No convergence

El	Nel	LS	N	ν	A [26] u_1	N u_1	A [26] u_2	N u_2	A [26] φ_3	N φ_3	CPU time
Hex8NL	16	150	0.5	200.0	-10.11	-12.10	0.01	1.22	6.19	5.22	18 sec
Hex8NLIM	16	150	0.5	200.0	-10.11	-10.23	0.01	-0.07	6.19	6.17	25 sec
Hex27NL	16	150	0.5	200.0	-10.11	x	0.01	x	6.19	x	NC
Hex8NL	32	150	0.5	200.0	-10.11	-10.80	0.01	0.16	6.19	5.91	35 sec
Hex8NLIM	32	150	0.5	200.0	-10.11	x	0.01	x	6.19	x	NC
Hex27NL	32	150	0.5	200.0	-10.11	x	0.01	x	6.19	x	NC
Hex8NL	16	150	0.9	2557.89	-10.11	-11.56	0.01	6.17	6.19	3.60	16 sec
Hex8NLIM	16	150	0.9	2557.89	-10.11	-10.67	0.01	-0.36	6.19	5.99	18 sec
Hex27NL	16	150	0.9	2557.89	-10.11	x	0.01	x	6.19	x	NC
Hex8NL	32	150	0.9	2557.89	-10.11	-12.16	0.01	1.20	6.19	5.21	32 sec
Hex8NLIM	32	150	0.9	2557.89	-10.11	-10.30	0.01	-0.20	6.19	6.13	41 sec
Hex27NL	32	150	0.9	2557.89	-10.11	x	0.01	x	6.19	x	NC

Next we want to check if the polar ratio ψ affects the solution. The polar ratio is chosen as $\psi \in \{0.1, 0.7, 1.4\}$ and the problem is solved first for $N = 0.5$ (Table 14) and then for $N = 0.9$ (Table 15). From the obtained results it can be concluded that parameter ψ does not affect the numerical solution.

Table 14: Variation of the polar ratio $\psi \in \{0.1, 0.7, 1.4\}$ for $E = 1200$ N/m^2, $n = 0.0$, $l_b = 0.15$ m, $l_t = 0.04$ m, $N = 0.5$: Results at node $P = (L, h, b)$, A = Analytical, N = Numerical, LS = Number of load steps, NC = No convergence

El	Nel	LS	ψ	α	A [26] u_1	N u_1	A [26] u_2	N u_2	A [26] φ_3	N φ_3	CPU time
Hex8NL	32	150	0.1	17.28	-10.11	-10.78	0.01	0.16	6.19	5.91	35 sec
Hex8NLIM	32	150	0.1	17.28	-10.11	x	0.01	x	6.19	x	NC
Hex27NL	32	150	0.1	17.28	-10.11	x	0.01	x	6.19	x	NC
Hex8NL	32	150	0.7	0.823	-10.11	-10.78	0.01	0.16	6.19	5.91	35 sec
Hex8NLIM	32	150	0.7	0.823	-10.11	x	0.01	x	6.19	x	NC
Hex27NL	32	150	0.7	0.823	-10.11	x	0.01	x	6.19	x	NC
Hex8NL	32	150	1.4	-0.549	-10.11	-10.78	0.01	0.16	6.19	5.91	35 sec
Hex8NLIM	32	150	1.4	-0.549	-10.11	x	0.01	x	6.19	x	NC
Hex27NL	32	150	1.4	-0.549	-10.11	x	0.01	x	6.19	x	NC

Table 15: Variation of the polar ratio $\psi \in \{0.1, 0.7, 1.4\}$ for $E = 1200$ N/m^2, $n = 0.0$, $l_b = 0.15$ m, $l_t = 0.04$ m, $N = 0.9$: Results at node $P = (L, h, b)$, A = Analytical, N = Numerical, LS = Number of load steps, NC = No convergence

El	Nel	LS	ψ	α	A [26] u_1	N u_1	A [26] u_2	N u_2	A [26] φ_3	N φ_3	CPU time
Hex8NL	32	150	0.1	17.28	-10.11	-12.16	0.01	1.12	6.19	5.21	32 sec
Hex8NLIM	32	150	0.1	17.28	-10.11	-10.30	0.01	-0.20	6.19	6.13	42 sec
Hex8NL	32	150	0.7	0.823	-10.11	-12.16	0.01	1.12	6.19	5.21	32 sec
Hex8NLIM	32	150	0.7	0.823	-10.11	-10.30	0.01	-0.20	6.19	6.13	42 sec
Hex8NL	32	150	1.4	-0.549	-10.11	-12.16	0.01	1.12	6.19	5.21	32 sec
Hex8NLIM	32	150	1.4	-0.549	-10.11	-10.30	0.01	-0.20	6.19	6.13	42 sec

Finally, we vary the value of the characteristic torsion length $l_t \in \{0.1, 0.5, 0.9\}$ and keep the values of the coupling number and polar ratio fixed and equal to $N = 0.9$ and $\psi = 1.0$. Again, from Table 16 it can be seen that the value of the characteristic torsion length does not affect the numerical solution (and the deformed configuration).

Table 16: Variation of the characteristic torsion length $l_t \in [0.1, 0.5, 0.9]$ for $E = 1200$ N/m^2, $n = 0.0$, $l_b = 0.15$ m, $\psi = 1.0$, $N = 0.9$: Results at node $P = (L, h, b)$, A = Analytical, N = Numerical, LS = Number of load steps, NC = No convergence

El	Nel	LS	l_t	β	γ	A [26] u_1	N u_1	A [26] u_2	N u_2	A [26] φ_3	N φ_3	CPU time
Hex8NL	32	150	0.1	6.0	48.0	-10.11	-12.16	0.01	1.20	6.19	5.21	32 sec
Hex8NLIM	32	150	0.1	6.0	48.0	-10.11	-10.30	0.01	-0.20	6.19	6.13	42 sec
Hex8NL	32	150	0.5	150.0	-96.0	-10.11	-12.16	0.01	1.20	6.19	5.21	32 sec
Hex8NLIM	32	150	0.5	150.0	-96.0	-10.11	-10.30	0.01	-0.20	6.19	6.13	41 sec
Hex8NL	32	150	0.9	486.0	-432.0	-10.11	-12.16	0.01	1.20	6.19	5.21	32 sec
Hex8NLIM	32	150	0.9	486.0	-432.0	-10.11	-10.30	0.01	-0.20	6.19	6.13	41 sec

4.2. 45° degree curved cantilever bend

A genuine three-dimensional problem will be analysed next in order to test the element ability to model large three-dimensional rotations. A curved cantilever beam with out-of-plane loading first presented in [28] is modeled using the geometrically nonlinear Lagrange elements presented in [18] and the newly presented enhanced Hex8NLIM element.

The beam of constant curvature with a radius $R = 100$ forming a 45° arc lies in a horizontal plane, as shown in Figure 9. The cantilever is loaded normally to that plane at the free end by a constant distributed surface loading $p_3 = 600$ along the square-shaped cross-section of the side $a = 1$. The distributed surface loading is applied through corresponding concentrated nodal forces in a number of load increments. The cantilever is clamped at the left-hand side end, i.e. all the displacements and microrotations are restrained ($u_1(0, x_2, x_3) = u_2(0, x_2, x_3) = u_3(0, x_2, x_3) = \varphi_1(0, x_2, x_3) = \varphi_2(0, x_2, x_3) = \varphi_3(0, x_2, x_3) = 0$, for $x_2 \in [R - 0.5a, R + 0.5a]$, and $x_3 \in [0, a]$).

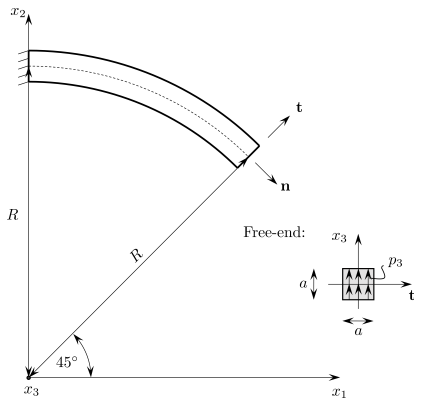

Figure 9: Top view of the curved cantilever beam

The obtained numerical results are compared against a reference numerical solution of the classical theory [20].

Lamé constants are taken as in [20], i.e. $\mu = 5 \cdot 10^6$, $\lambda = 0$. The remaining material parameters are chosen as $\nu = 50\ 505.1$, $\alpha = 0$, $\beta = 12\ 500$ and $\gamma = 37\ 500$, which correspond to the following engineering material parameters: $E = 10^7$, $n = 0.0$, $N = 0.1$, $l_b = 0.05$, $l_t = 0.05$, $\psi = 1$. Thus, the engineering material parameters describing the contribution of the microstructure are taken as small, so that the obtained results could be compared to the solution available in the framework of the classical elasticity. The problem is solved by using a finite element mesh of 16 elements propagating in the longitudinal direction. The obtained results at nodes $P_1 = (70.357, 70.357, 0.0)$, $P_2 = (71.064, 71.064, 0.0)$, $P_3 = (70.357, 70.357, 1.0)$ and $P_4 = (71.064, 71.064, 1.0)$ are then averaged and given in Table 17.

It can be observed that the first-order element performs poorly for such a coarse mesh, while the results obtained using Hex8NLIM and Hex27NL are very close to the reference solution, but slightly stiffer due to the existence of micropolar effects in the model. However, the computational time needed to obtain the result using Hex8NLIM is 30 times lower than that needed for the Hex27NL element.

Table 17: Obtained numerical results for the curved cantilever bend problem

(a) $16 \times 1 \times 1$ Hex8NL elements

El	Nel	LS	Node	u_1	u_2	u_3	$\varphi_1 \cdot 10^{-1}$	$\varphi_2 \cdot 10^{-2}$	$\varphi_3 \cdot 10^{-2}$
Hex8NL	16	1	P_1	-1.28	1.91	16.06	-5.08	-6.06	-3.56
			P_2	-1.24	1.80	15.76	-5.08	-6.06	-3.57
			P_3	-1.32	2.40	15.93	-5.08	-6.06	-3.57
			P_4	-1.28	2.29	15.63	-5.08	-6.06	-3.57
Averaged results				-1.28	2.10	15.85	-5.08	-6.06	-3.57
Hex8NLIM	16	7	P_1	-22.03	12.92	52.67	-5.67	-9.85	-5.85
			P_2	-22.20	13.02	52.89	-5.67	-9.85	-5.85
			P_3	-22.83	13.33	52.08	-5.67	-9.85	-5.86
			P_4	-23.01	13.44	52.31	-5.67	-9.85	-5.85
Averaged results				-22.52	13.18	52.49	-5.67	-9.85	-5.85
Hex27NL	16	7	P_1	-22.05	12.85	52.70	-5.65	-9.87	-5.56
			P_2	-22.20	13.02	52.89	-5.65	-9.87	-5.58
			P_3	-22.83	13.33	52.08	-5.65	-9.87	-5.58
			P_4	-23.01	13.44	52.31	-5.65	-9.87	-5.57
Averaged results				-22.54	13.11	52.52	-5.67	-9.87	-5.57
Ref. solution [20]				-23.30	13.64	53.21	-	-	-

5. Conclusion

In the scope of this work a new three-dimensional geometrically non-linear enhanced micropolar finite element has been derived. The element is based on Biot-like stress and strain tensors with a linear elastic isotropic constitutive law.

The numerical implementation of the finite element is performed within the Finite Element Analysis Program (FEAP) [25]. The finite-element performance has been tested on several numerical examples in the geometrically non-linear regime consisting of a pure-bending problem and a full 3D deformation problem. Regarding the pure-bending problem, it is observed that the newly developed finite element reproduces the analytical solution [26] for a coarse mesh. Furthermore, it is observed that it is significantly more accurate than the first-order Lagrangian element, and more robust and remarkably more efficient than the second-order Lagrangian finite element developed in [18], especially so for thin beams. The element is able to describe high curvature deformation in a reasonable computational time, which is not the case for the Lagrangian elements developed in [18].

Also, a micropolar parameter sensitivity analysis has been performed within this example, where the values of parameters not existing in the analytical solution of the pure bending problem (the coupling number, polar ratio and characteristic torsion length) have been varied. It is observed that the coupling number affects both the precision and robustness of the numerical solution. However, the values of the polar ratio and the characteristic bending length do not affect the solution in either way.

A genuine 3D problem consisting of a curved cantilever beam subject to out-of-plane loading is modelled. It is observed that the solution obtained with the newly presented element requires significantly lower computational time than the second-order element (around 30 times lower), with the same precision. It is concluded that the hexahedral geometrically-nonlinear micropolar finite element with incompatible-mode enhancement in the displacement field is an efficient and robust micropolar finite element, highly suitable for modeling behavior of micropolar materials in the three-dimensional geometrically non-linear regime.

Acknowledgement

This work has been financially supported by the Croatian Science Foundation research project "Fixed-Pole Concept in Numerical Modelling of Cosserat Continuum" (HRZZ-IP-2018-01-1732) and the University of Rijeka Young Researchers grant "Analysis of the pure bending problem in the geometrically non-linear micropolar continuum theory" (uniri-mladi-tehnic-22-482835).

Appendix A. Derivation of terms needed in the incompatible modes residual

Appendix A.1. Term $\lambda\mathbf{Q}\left(M_a\nabla_X\right)tr(\mathbf{E})$

$$\lambda\mathbf{Q}\left(M_a\nabla_X\right)\mathrm{tr}(\mathbf{E}) \tag{A.1}$$

$$\begin{aligned}
&= \lambda\mathbf{Q}\left(M_a\nabla_X\right)\mathrm{tr}\left(\mathbf{Q}^{\mathrm{T}}\mathbf{F}-\mathbf{I}\right)\\
&= \lambda\mathbf{Q}\left(M_a\nabla_X\right)\mathrm{tr}\left(\mathbf{Q}^{\mathrm{T}}\mathbf{F}\right)-\lambda\mathbf{Q}\left(M_a\nabla_X\right)\mathrm{tr}\left(\mathbf{I}\right)\\
&= \lambda\mathbf{Q}\left(M_a\nabla_X\right)\mathrm{tr}\left(\mathbf{Q}^{\mathrm{T}}\left(\mathrm{GRAD}\mathbf{u}+\mathbf{I}\right)\right)-3\lambda\mathbf{Q}\left(M_a\nabla_X\right)\\
&= \lambda\mathbf{Q}\left(M_a\nabla_X\right)\mathrm{tr}\left(\mathbf{Q}^{\mathrm{T}}\mathbf{u}\nabla_X^{\mathrm{T}}\right)+\lambda\mathbf{Q}\left(M_a\nabla_X\right)\mathrm{tr}\left(\mathbf{Q}^{\mathrm{T}}\right)-3\lambda\mathbf{Q}\left(M_a\nabla_X\right)\\
&= \lambda\mathbf{Q}\left(M_a\nabla_X\right)\nabla_X\cdot\mathbf{Q}^{\mathrm{T}}\mathbf{u}+\lambda\mathbf{Q}\left(M_a\nabla_X\right)\mathrm{tr}\left(\mathbf{Q}^{\mathrm{T}}\right)-3\lambda\mathbf{Q}\left(M_a\nabla_X\right)\\
&= \lambda\mathbf{Q}\left(M_a\nabla_X\right)\nabla_X^{\mathrm{T}}\mathbf{Q}^{\mathrm{T}}\mathbf{u}+\lambda\mathbf{Q}\left(M_a\nabla_X\right)\mathrm{tr}\left(\mathbf{Q}^{\mathrm{T}}\right)-3\lambda\mathbf{Q}\left(M_a\nabla_X\right)\\
&= \lambda\mathbf{Q}\left(M_a\nabla_X\right)\nabla_X^{\mathrm{T}}\mathbf{Q}^{\mathrm{T}}\left(\sum_{i=1}^{8}N_i(\xi,\eta,\zeta)\mathbf{u}_i^e+\sum_{b=1}^{3}M_b(\xi,\eta,\zeta)\boldsymbol{\alpha}_b^e\right)+\lambda\mathbf{Q}\left(M_a\nabla_X\right)\mathrm{tr}\left(\mathbf{Q}^{\mathrm{T}}\right)-3\lambda\mathbf{Q}\left(M_a\nabla_X\right),
\end{aligned} \tag{A.2}$$

where ∇_X^{T} from the first term operates on N_i and M_b.

Appendix A.2. Term $(\mu+\nu)\mathbf{Q}\mathbf{E}\left(M_a\nabla_X\right)$

$$
\begin{aligned}
&(\mu+\nu)\mathbf{Q}\mathbf{E}(M_a\nabla_X) \qquad \text{(A.3)}\\
&= (\mu+\nu)\mathbf{Q}\left(\mathbf{Q}^{\mathrm{T}}\mathbf{F}-\mathbf{I}\right)\left(M_a\nabla_X\right)\\
&= (\mu+\nu)\mathbf{Q}\mathbf{Q}^{\mathrm{T}}\mathbf{F}(M_a\nabla_X)-(\mu+\nu)\mathbf{Q}(M_a\nabla_X)\\
&= (\mu+\nu)\left(\mathrm{GRAD}\mathbf{u}+\mathbf{I}\right)\left(M_a\nabla_X\right)-(\mu+\nu)\mathbf{Q}(M_a\nabla_X)\\
&= (\mu+\nu)\left(\mathbf{u}\otimes\nabla_X\right)\left(M_a\nabla_X\right)+(\mu+\nu)\mathbf{I}(M_a\nabla_X)-(\mu+\nu)\mathbf{Q}(M_a\nabla_X)\\
&= (\mu+\nu)\left(\mathbf{u}\underbrace{\nabla_X^{\mathrm{T}}M_a\nabla_X}_{scalar}\right)+(\mu+\nu)\mathbf{I}(M_a\nabla_X)-(\mu+\nu)\mathbf{Q}(M_a\nabla_X)\\
&= (\mu+\nu)\left(\nabla_X^{\mathrm{T}}M_a\nabla_X\right)\mathbf{u}+(\mu+\nu)\mathbf{I}(M_a\nabla_X)-(\mu+\nu)\mathbf{Q}(M_a\nabla_X)\\
&= (\mu+\nu)\left(\nabla_X^{\mathrm{T}}M_a\nabla_X\right)\left(\sum_{i=1}^{8}N_i(\xi,\eta,\zeta)\mathbf{u}_i^e+\sum_{b=1}^{3}M_b(\xi,\eta,\zeta)\boldsymbol{\alpha}_b^e\right)+(\mu+\nu)\mathbf{I}(M_a\nabla_X)-(\mu+\nu)\mathbf{Q}(M_a\nabla_X)\\
&\qquad\qquad \text{(A.4)}
\end{aligned}
$$

where ∇_X^{T} in (A.4) operates on N_i and M_b.

Appendix A.3. Term $(\mu-\nu)\mathbf{Q}\mathbf{E}^T\left(M_a\nabla_X\right)$

$$
\begin{aligned}
&(\mu-\nu)\mathbf{Q}\mathbf{E}^{\mathrm{T}}(M_a\nabla_X) \qquad \text{(A.5)}\\
&= (\mu-\nu)\mathbf{Q}\left(\mathbf{F}^{\mathrm{T}}\mathbf{Q}-\mathbf{I}\right)\left(M_a\nabla_X\right)\\
&= (\mu-\nu)\mathbf{Q}\left(\mathrm{GRAD}\mathbf{u}+\mathbf{I}\right)^{\mathrm{T}}\mathbf{Q}(M_a\nabla_X)-(\mu-\nu)\mathbf{Q}(M_a\nabla_X)\\
&= (\mu-\nu)\mathbf{Q}\left(\mathbf{u}\nabla_X^{\mathrm{T}}\right)^{\mathrm{T}}\mathbf{Q}(M_a\nabla_X)+(\mu-\nu)\mathbf{Q}\mathbf{Q}(M_a\nabla_X)-(\mu-\nu)\mathbf{Q}(M_a\nabla_X)\\
&= (\mu-\nu)\mathbf{Q}\nabla_X\mathbf{u}^{\mathrm{T}}\mathbf{Q}(M_a\nabla_X)+(\mu-\nu)\mathbf{Q}\mathbf{Q}(M_a\nabla_X)-(\mu-\nu)\mathbf{Q}(M_a\nabla_X)\\
&= (\mu-\nu)\mathbf{Q}\nabla_X(M_a\nabla_X^{\mathrm{T}})\mathbf{Q}^{\mathrm{T}}\mathbf{u}+(\mu-\nu)\mathbf{Q}\mathbf{Q}(M_a\nabla_X)-(\mu-\nu)\mathbf{Q}(M_a\nabla_X)\\
&= (\mu-\nu)\mathbf{Q}\nabla_X(M_a\nabla_X^{\mathrm{T}})\mathbf{Q}^{\mathrm{T}}\left(\sum_{i=1}^{8}N_i(\xi,\eta,\zeta)\mathbf{u}_i^e+\sum_{b=1}^{3}M_b(\xi,\eta,\zeta)\boldsymbol{\alpha}_b^e\right)+(\mu-\nu)\mathbf{Q}\mathbf{Q}(M_a\nabla_X)-(\mu-\nu)\mathbf{Q}(M_a\nabla_X\\
&\qquad\qquad \text{(A.6)}
\end{aligned}
$$

where ∇_X from the first term operates on N_i and M_b.

Appendix B. Derivation of terms needed in the linearized residuals

Appendix B.1. Matrix K^e

In the nonlinear analysis $\mathbf{K}^e$ consists of two parts:

$$\mathbf{K}^e = {\mathbf{K}_\mathrm{M}}^e + {\mathbf{K}_\mathrm{G}}^e. \tag{B.1}$$

The matrix ${\mathbf{K}_\mathrm{M}}^e$ is referred to as the element material stiffness matrix and ${\mathbf{K}_\mathrm{G}}^e$ is referred to as the element geometric stiffness matrix. The part ${\mathbf{K}_\mathrm{M}}^e$ depends on material properties, while the part ${\mathbf{K}_\mathrm{G}}^e$ depends on stresses and is a characteristic of large displacement/rotation problems and consequently does not exist in the linear analysis.

The linearization of each term in the element residual is derived and presented in detail in [21] in Appendix G. By introducing the linearized terms derived there and substituting $\boldsymbol{\ell} = \mathrm{ax}(\mathrm{skew}(\mathbf{F}\mathbf{Q}^\mathrm{T}))$ we obtain the element incremental residual

$$\Delta\mathbf{g}^e = \begin{Bmatrix} \Delta\mathbf{g}_1^e \\ \Delta\mathbf{g}_2^e \\ \vdots \\ \Delta\mathbf{g}_{n_{node}}^e \end{Bmatrix}. \tag{B.2}$$

The element incremental nodal residual $\Delta\mathbf{g}_i^e$ is thus

$$\Delta\mathbf{g}_i^e = \int \begin{Bmatrix} \Delta\mathbf{g}_i^{e1} \\ \Delta\mathbf{g}_i^{e2} \end{Bmatrix} dV, \tag{B.3}$$

where vectors $\Delta\mathbf{g}_i^{e1}$ and $\Delta\mathbf{g}_i^{e2}$ are equal to

$$\begin{aligned} \Delta\mathbf{g}_i^{e1} &= \left(\widehat{\Delta\boldsymbol{\varphi}}\mathbf{Q}\mathbf{B} + \mathbf{Q}\left(\mathbf{T} : \Delta\mathbf{E}\right)\right)(N_i\nabla_X), \\ \Delta\mathbf{g}_i^{e2} &= \left(\widehat{\Delta\boldsymbol{\varphi}}\mathbf{Q}\mathbf{G} + \mathbf{Q}\left(\mathbf{D} : \Delta\mathbf{K}\right)\right)(N_i\nabla_X) \\ &\quad - N_i\boldsymbol{\epsilon} : \left(\mathrm{GRAD}\Delta\mathbf{u}\mathbf{B}^\mathrm{T}\mathbf{Q}^\mathrm{T} + \mathbf{F}(\mathbf{T} : \Delta\mathbf{E})^\mathrm{T}\mathbf{Q}^\mathrm{T} + \mathbf{F}\mathbf{B}^\mathrm{T}\mathbf{Q}^\mathrm{T}\widehat{\Delta\boldsymbol{\varphi}}^\mathrm{T}\right). \end{aligned} \tag{B.4}$$

Here, we introduce the equalities derived in [21] in Appendix G, as follows:

$$\begin{aligned}
&\left(\widehat{\Delta\boldsymbol{\varphi}}\mathbf{Q}\mathbf{B}+\mathbf{Q}\left(\mathbf{T}:\Delta\mathbf{E}\right)\right)\left(N_i\nabla_X\right)\\
&=\left(\lambda\mathbf{Q}(N_i\nabla_X)\nabla_X^{\mathrm{T}}\mathbf{Q}^{\mathrm{T}}+(\mu+\nu)\nabla_X^{\mathrm{T}}(N_i\nabla_X)\mathbf{I}+(\mu-\nu)\mathbf{Q}\nabla_X(N_i\nabla_X)^{\mathrm{T}}\mathbf{Q}^{\mathrm{T}}\right)\Delta\mathbf{u}\\
&+\Big(-\widehat{\mathbf{Q}\mathbf{B}(N_i\nabla_X)}+\lambda\mathbf{Q}(N_i\nabla_X)2\left[\mathrm{ax}(\mathrm{skew}(\mathbf{F}\mathbf{Q}^{\mathrm{T}}))\right]^{\mathrm{T}}+(\mu+\nu)\widehat{\mathbf{F}(N_i\nabla_X)}\\
&-(\mu-\nu)\mathbf{Q}\mathbf{F}^{\mathrm{T}}\widehat{\mathbf{Q}(N_i\nabla_X)}\Big)\Delta\boldsymbol{\varphi},
\end{aligned}\tag{B.5}$$

where free ∇_X in the factor multiplying $\Delta\mathbf{u}$ operates exclusively on $\Delta\mathbf{u}$,

$$\begin{aligned}
&\left(\widehat{\Delta\boldsymbol{\varphi}}\mathbf{Q}\mathbf{G}+\mathbf{Q}\left(\mathbf{D}:\Delta\mathbf{K}\right)\right)\left(N_i\nabla_X\right)\\
&=\Big(-\widehat{\mathbf{Q}\mathbf{G}(N_i\nabla_X)}+\alpha\mathbf{Q}(N_i\nabla_X)\nabla_X^{\mathrm{T}}\mathbf{Q}^{\mathrm{T}}+(\beta+\gamma)\nabla_X^{\mathrm{T}}(N_i\nabla_X)+(\beta-\gamma)\mathbf{Q}\nabla_X(N_i\nabla_X)^{\mathrm{T}}\mathbf{Q}^{\mathrm{T}}\Big)\Delta\boldsymbol{\varphi},
\end{aligned}\tag{B.6}$$

where free ∇_X in the factor multiplying $\Delta\boldsymbol{\varphi}$ operates exclusively on $\Delta\boldsymbol{\varphi}$ and

$$\begin{aligned}
&-N_i\boldsymbol{\epsilon}:\Big(\mathrm{GRAD}\Delta\mathbf{u}\mathbf{B}^{\mathrm{T}}\mathbf{Q}^{\mathrm{T}}+\mathbf{F}(\mathbf{T}:\Delta\mathbf{E})^{\mathrm{T}}\mathbf{Q}^{\mathrm{T}}+\mathbf{F}\mathbf{B}^{\mathrm{T}}\mathbf{Q}^{\mathrm{T}}\widehat{\Delta\boldsymbol{\varphi}}^{\mathrm{T}}\Big)\\
&=N_i\widehat{\mathbf{Q}\mathbf{B}\nabla_X}\Delta\mathbf{u}+4\lambda N_i\ \mathrm{ax}(\mathrm{skew}(\mathbf{F}\mathbf{Q}^{\mathrm{T}}))\left[\mathrm{ax}(\mathrm{skew}(\mathbf{F}\mathbf{Q}^{\mathrm{T}}))\right]^{\mathrm{T}}\Delta\boldsymbol{\varphi}\\
&+2\lambda N_i\ \mathrm{ax}(\mathrm{skew}(\mathbf{F}\mathbf{Q}^{\mathrm{T}}))\nabla_X^{\mathrm{T}}\mathbf{Q}^{\mathrm{T}}\Delta\mathbf{u}-(\mu+\nu)N_i\left(\mathbf{F}\mathbf{F}^{\mathrm{T}}-\mathrm{tr}(\mathbf{F}\mathbf{F}^{\mathrm{T}})\mathbf{I}\right)\Delta\boldsymbol{\varphi}\\
&-(\mu+\nu)N_i\widehat{\mathbf{F}\nabla_X}\Delta\mathbf{u}\\
&+(\mu-\nu)N_i\left[\mathbf{m_1}\ \ \mathbf{m_2}\ \ \mathbf{m_3}\right]\Delta\boldsymbol{\varphi}\\
&+(\mu-\nu)N_i\widehat{\mathbf{Q}\nabla_X}\mathbf{F}\mathbf{Q}^{\mathrm{T}}\Delta\mathbf{u}+N_i\left[\left(\mathbf{F}\mathbf{B}^{\mathrm{T}}\mathbf{Q}^{\mathrm{T}}\right)^{\mathrm{T}}-\mathrm{tr}\left(\mathbf{F}\mathbf{B}^{\mathrm{T}}\mathbf{Q}^{\mathrm{T}}\right)\mathbf{I}\right]\Delta\boldsymbol{\varphi},
\end{aligned}\tag{B.7}$$

where $\mathbf{m_i}=\mathrm{ax}(2\mathrm{skew}(\mathbf{F}\mathbf{Q}^{\mathrm{T}}\boldsymbol{\epsilon_i}\mathbf{F}\mathbf{Q}^{\mathrm{T}}))$ and $\boldsymbol{\epsilon_i}$ is a submatrix of the Levi-Civita tensor. In (B.7) all ∇_X operate on $\Delta\mathbf{u}$.

Finally, we obtain the vectors $\Delta\mathbf{g}_i^{e1}$ and $\Delta\mathbf{g}_i^{e2}$ as

$$\begin{aligned}\Delta\mathbf{g}_i^{e1} =& -\widehat{\mathbf{QB}(N_i\nabla_X)}\Delta\boldsymbol{\varphi} + \lambda\mathbf{Q}(N_i\nabla_X)2\boldsymbol{\ell}^{\mathrm{T}}\Delta\boldsymbol{\varphi} + \lambda\mathbf{Q}(N_i\nabla_X)\nabla_X^{\mathrm{T}}\mathbf{Q}^{\mathrm{T}}\Delta\mathbf{u}\\ &+ (\mu+\nu)\widehat{\mathbf{F}(N_i\nabla_X)}\Delta\boldsymbol{\varphi} + (\mu+\nu)\nabla_X^{\mathrm{T}}(N_i\nabla_X)\Delta\mathbf{u}\\ &- (\mu-\nu)\mathbf{Q}\mathbf{F}^{\mathrm{T}}\widehat{\mathbf{Q}(N_i\nabla_X)}\Delta\boldsymbol{\varphi} + (\mu-\nu)\mathbf{Q}\nabla_X(N_i\nabla_X^{\mathrm{T}})\mathbf{Q}^{\mathrm{T}}\Delta\mathbf{u}, \end{aligned} \tag{B.8}$$

$$\begin{aligned}\Delta\mathbf{g}_i^{e2} =& -\widehat{\mathbf{QG}(N_i\nabla_X)}\Delta\boldsymbol{\varphi} + \alpha\mathbf{Q}(N_i\nabla_X)\nabla_X^{\mathrm{T}}\mathbf{Q}^{\mathrm{T}}\Delta\boldsymbol{\varphi} + (\beta+\gamma)\nabla_X^{\mathrm{T}}(N_i\nabla_X)\Delta\boldsymbol{\varphi}\\ &+ (\beta-\gamma)\mathbf{Q}\nabla_X(N_i\nabla_X^{\mathrm{T}})\mathbf{Q}^{\mathrm{T}}\Delta\boldsymbol{\varphi} + N_i\widehat{\mathbf{QB}\nabla_X}\Delta\mathbf{u} + 4\lambda N_i\,\boldsymbol{\ell}\boldsymbol{\ell}^{\mathrm{T}}\Delta\boldsymbol{\varphi}\\ &+ 2\lambda N_i\,\boldsymbol{\ell}\nabla_X^{\mathrm{T}}\mathbf{Q}^{\mathrm{T}}\Delta\mathbf{u} - (\mu+\nu)N_i\left(\mathbf{F}\mathbf{F}^{\mathrm{T}} - \mathrm{tr}(\mathbf{F}\mathbf{F}^{\mathrm{T}})\mathbf{I}\right)\Delta\boldsymbol{\varphi} - (\mu+\nu)N_i\widehat{\mathbf{F}\nabla_X}\Delta\mathbf{u}\\ &+ (\mu-\nu)N_i\left[\mathbf{m_1}\ \mathbf{m_2}\ \mathbf{m_3}\right]\Delta\boldsymbol{\varphi} + (\mu-\nu)N_i\widehat{\mathbf{Q}\nabla_X}\mathbf{F}\mathbf{Q}^{\mathrm{T}}\Delta\mathbf{u}\\ &+ N_i\left[\left(\mathbf{F}\mathbf{B}^{\mathrm{T}}\mathbf{Q}^{\mathrm{T}}\right)^{\mathrm{T}} - \mathrm{tr}\left(\mathbf{F}\mathbf{B}^{\mathrm{T}}\mathbf{Q}^{\mathrm{T}}\right)\mathbf{I}\right]\Delta\boldsymbol{\varphi}. \end{aligned} \tag{B.9}$$

Next, we split the element incremental nodal residual $\Delta\mathbf{g}_i^e$ into its geometric and material part as:

$$\Delta\mathbf{g}_i^e = \Delta\mathbf{g}_{\mathrm{G}_i}^e + \Delta\mathbf{g}_{\mathrm{M}_i}^e. \tag{B.10}$$

In order to obtain the geometric element stiffness matrix, we observe the part of the element incremental residual $\mathbf{g}_{\mathrm{G}_i}^e$ which depends on stresses $\mathbf{B}$ and/or $\mathbf{G}$ which is equal to:

$$\Delta\mathbf{g}_{\mathrm{G}_i}^e = \int_V \begin{Bmatrix}\Delta\mathbf{g}_{\mathrm{G}_i}^{e1}\\ \Delta\mathbf{g}_{\mathrm{G}_i}^{e2}\end{Bmatrix} dV, \tag{B.11}$$

where vectors $\Delta\mathbf{g}_{\mathrm{G}_i}^{e1}$ and $\Delta\mathbf{g}_{\mathrm{G}_i}^{e2}$ are equal to

$$\Delta\mathbf{g}_{\mathrm{G}_i}^{e1} = \left(-\widehat{\mathbf{QB}(N_i\nabla_X)} + 2\lambda\mathbf{Q}(N_i\nabla_X)\boldsymbol{\ell}^{\mathrm{T}}\right)\Delta\boldsymbol{\varphi}, \tag{B.12}$$

$$\begin{aligned}\Delta\mathbf{g}_{\mathrm{G}_i}^{e2} =& \left(-\widehat{\mathbf{QG}(N_i\nabla_X)} + 4\lambda N_i\boldsymbol{\ell}\boldsymbol{\ell}^{\mathrm{T}} + N_i\left[(\mathbf{F}\mathbf{B}^{\mathrm{T}}\mathbf{Q}^{\mathrm{T}})^{\mathrm{T}} - \mathrm{tr}(\mathbf{F}\mathbf{B}^{\mathrm{T}}\mathbf{Q}^{\mathrm{T}})\mathbf{I}\right]\right)\Delta\boldsymbol{\varphi}\\ &+ \left(N_i\widehat{\mathbf{QB}\nabla_X} + 2\lambda N_i\boldsymbol{\ell}\nabla_X^{\mathrm{T}}\mathbf{Q}^{\mathrm{T}}\right)\Delta\mathbf{u}. \end{aligned} \tag{B.13}$$

It is important to note that terms $\lambda\mathbf{Q}(N_i\nabla_X)\boldsymbol{\ell}^{\mathrm{T}}\Delta\boldsymbol{\varphi}$, $4\lambda N_i\boldsymbol{\ell}\boldsymbol{\ell}^{\mathrm{T}}$ and $2\lambda N_i\boldsymbol{\ell}\nabla_X^{\mathrm{T}}\mathbf{Q}^{\mathrm{T}}\Delta\mathbf{u}$ contain the material parameter λ and as such is more intuitive to be classified as terms belonging to the material part. However, in the linear analysis of the

present formulation these three terms vanish, which is the reason why we classified them as a part of the geometric stiffness. By extracting the vector of incremental displacements and microrotations we obtain

$$\Delta \mathbf{g}^e_{\mathrm{G}_i} = \int_V \begin{bmatrix} \mathbf{0} & -\widehat{\mathbf{QB}(N_i\nabla_X)} + 2\lambda \mathbf{Q}(N_i\nabla_X)\boldsymbol{\ell}^{\mathrm{T}} \\ N_i\widehat{\mathbf{QB}\nabla_X} + 2\lambda N_i \boldsymbol{\ell}\nabla_X^{\mathrm{T}}\mathbf{Q}^{\mathrm{T}} & -\widehat{\mathbf{QG}(N_i\nabla_X)} + 4\lambda N_i \boldsymbol{\ell}\boldsymbol{\ell}^{\mathrm{T}} + N_i\left[(\mathbf{F}\mathbf{B}^{\mathrm{T}}\mathbf{Q}^{\mathrm{T}})^{\mathrm{T}} - \mathrm{tr}(\mathbf{F}\mathbf{B}^{\mathrm{T}}\mathbf{Q}^{\mathrm{T}})\mathbf{I}\right] \end{bmatrix} \begin{Bmatrix} \Delta\mathbf{u} \\ \Delta\boldsymbol{\varphi} \end{Bmatrix} dV, \tag{B.14}$$

where $\mathbf{0}$ is a 3×3 zero matrix. Now we introduce into (B.14) the interpolation of the kinematic field increments defined earlier as

$$\Delta\mathbf{u}^h = \sum_{j=1}^{n_{node}} N_j(\xi,\eta,\zeta)\Delta\mathbf{u}_j, \qquad \Delta\boldsymbol{\varphi}^h = \sum_{j=1}^{n_{node}} N_j(\xi,\eta,\zeta)\Delta\boldsymbol{\varphi}_j, \tag{B.15}$$

and by extracting the interpolated vector of incremental nodal degrees of freedom $\Delta\mathbf{d}^e_j = \begin{Bmatrix} \Delta\mathbf{u} \\ \Delta\boldsymbol{\varphi} \end{Bmatrix}$ we obtain

$$\Delta\mathbf{g}^e_{\mathrm{G}_i} = \sum_{j=1}^{n_{node}} \mathbf{K}_{\mathrm{G}}{}^e_{ij}\Delta\mathbf{d}^e_j, \tag{B.16}$$

where the 6×6 element block geometric stiffness matrix $\mathbf{K}_{\mathrm{G}}{}^e_{ij}$ follows as

$$\mathbf{K}_{\mathrm{G}}{}^e_{ij} = \int_V \begin{bmatrix} \mathbf{0} & \mathbf{K}_{\mathrm{G}}{}^{e1}_{ij} \\ \mathbf{K}_{\mathrm{G}}{}^{e2}_{ij} & \mathbf{K}_{\mathrm{G}}{}^{e3}_{ij} \end{bmatrix} dV, \tag{B.17}$$

where the submatrices are

$$\mathbf{K}_{\mathrm{G}}{}^{e1}_{ij} = -\widehat{\mathbf{QB}(N_i\nabla_X)}N_j + 2\lambda\mathbf{Q}(N_i\nabla_X)\boldsymbol{\ell}^{\mathrm{T}}N_j, \tag{B.18}$$

$$\mathbf{K}_{\mathrm{G}}{}^{e2}_{ij} = N_i\widehat{\mathbf{QB}(N_j\nabla_X)} + 2\lambda N_i\boldsymbol{\ell}(N_j\nabla_X)^{\mathrm{T}}\mathbf{Q}^{\mathrm{T}}, \tag{B.19}$$

$$\mathbf{K}_{\mathrm{G}}{}^{e3}_{ij} = -\widehat{\mathbf{QG}(N_i\nabla_X)}N_j + 4\lambda N_iN_j\boldsymbol{\ell}\boldsymbol{\ell}^{\mathrm{T}} + N_iN_j\left[(\mathbf{F}\mathbf{B}^{\mathrm{T}}\mathbf{Q}^{\mathrm{T}})^{\mathrm{T}} - \mathrm{tr}(\mathbf{F}\mathbf{B}^{\mathrm{T}}\mathbf{Q}^{\mathrm{T}})\mathbf{I}\right]. \tag{B.20}$$

Next we define the element nodal incremental material residual $\Delta\mathbf{g}^e_{\mathrm{M}_i}$ as

$$\Delta\mathbf{g}^e_{\mathrm{M}_i} = \int_V \begin{Bmatrix} \Delta\mathbf{g}^{e1}_{\mathrm{M}_i} \\ \Delta\mathbf{g}^{e2}_{\mathrm{M}_i} \end{Bmatrix} dV, \tag{B.21}$$

where vectors $\Delta\mathbf{g}^{e1}_{\mathrm{M}_i}$ and $\Delta\mathbf{g}^{e2}_{\mathrm{M}_i}$ are equal to

$$\begin{aligned}\Delta\mathbf{g}^{e1}_{\mathrm{M}_i} =& \left(\lambda\mathbf{Q}(N_i\nabla_X)\nabla_X^{\mathrm{T}}\mathbf{Q}^{\mathrm{T}} + (\mu+\nu)\nabla_X^{\mathrm{T}}(N_i\nabla_X)\mathbf{I} + (\mu-\nu)\mathbf{Q}\nabla_X(N_i\nabla_X)^{\mathrm{T}}\mathbf{Q}^{\mathrm{T}}\right)\Delta\mathbf{u} \\ &+ \left((\mu+\nu)\widehat{\mathbf{F}(N_i\nabla_X)} - (\mu-\nu)\mathbf{Q}\mathbf{F}^{\mathrm{T}}\widehat{\mathbf{Q}(N_i\nabla_X)}\right)\Delta\boldsymbol{\varphi},\end{aligned} \tag{B.22}$$

$$\begin{aligned}\Delta\mathbf{g}^{e2}_{\mathrm{M}_i} =& \left(-(\mu+\nu)N_i\widehat{\mathbf{F}\nabla_X} + (\mu-\nu)N_i\widehat{\mathbf{Q}\nabla_X}\mathbf{F}\mathbf{Q}^{\mathrm{T}}\right)\Delta\mathbf{u} \\ &+ \left(\alpha\mathbf{Q}(N_i\nabla_X)\nabla_X^{\mathrm{T}}\mathbf{Q}^{\mathrm{T}} + (\beta+\gamma)\nabla_X^{\mathrm{T}}(N_i\nabla_X)\mathbf{I} + (\beta-\gamma)\mathbf{Q}\nabla_X(N_i\nabla_X^{\mathrm{T}})\mathbf{Q}^{\mathrm{T}}\right. \\ &\left.-(\mu+\nu)N_i\left(\mathbf{F}\mathbf{F}^{\mathrm{T}} - \mathrm{tr}(\mathbf{F}\mathbf{F}^{\mathrm{T}})\mathbf{I}\right) + (\mu-\nu)N_i\left[\mathbf{m_1}\ \mathbf{m_2}\ \mathbf{m_3}\right]\right)\Delta\boldsymbol{\varphi}.\end{aligned} \tag{B.23}$$

By extracting the vector of incremental displacements and microrotations and introducing the interpolation of the kinematic field increments defined in equation (B.15) into (B.21) and extracting $\Delta\mathbf{d}^e_j$ we obtain

$$\Delta\mathbf{g}^e_{\mathrm{M}_i} = \sum_{j=1}^{n_{node}} \mathbf{K}_{\mathrm{M}}{}^e_{ij}\Delta\mathbf{d}^e_j, \tag{B.24}$$

where the 6×6 element block material stiffness matrix $\mathbf{K}_{\mathrm{M}}{}^e_{ij}$ follows as

$$\mathbf{K}_{\mathrm{M}}{}^e_{ij} = \int_V \begin{bmatrix} \mathbf{K}_{\mathrm{M}}{}^{e1}_{ij} & \mathbf{K}_{\mathrm{M}}{}^{e2}_{ij} \\ \mathbf{K}_{\mathrm{M}}{}^{e3}_{ij} & \mathbf{K}_{\mathrm{M}}{}^{e4}_{ij} \end{bmatrix} dV, \tag{B.25}$$

where the submatrices are

$$\begin{aligned}\mathbf{K}_{\mathrm{M}}{}^{e1}_{ij} =& \lambda\mathbf{Q}(N_i\nabla_X)(N_j\nabla_X)^{\mathrm{T}}\mathbf{Q}^{\mathrm{T}} + (\mu+\nu)(N_j\nabla_X)^{\mathrm{T}}(N_i\nabla_X)\mathbf{I} \\ &+ (\mu-\nu)\mathbf{Q}(N_j\nabla_X)(N_i\nabla_X)^{\mathrm{T}}\mathbf{Q}^{\mathrm{T}}\end{aligned} \tag{B.26}$$

$$\mathbf{K}_{\mathrm{M}}{}^{e2}_{ij} = (\mu+\nu)\widehat{\mathbf{F}(N_i\nabla_X)}N_j - (\mu-\nu)\mathbf{Q}\mathbf{F}^{\mathrm{T}}\widehat{\mathbf{Q}(N_i\nabla_X)}N_j, \tag{B.27}$$

$$\mathbf{K}_{\mathrm{M}}{}^{e3}_{ij} = -(\mu+\nu)N_i\widehat{\mathbf{F}(N_j\nabla_X)} + (\mu-\nu)N_i\widehat{\mathbf{Q}(N_j\nabla_X)}\mathbf{F}\mathbf{Q}^{\mathrm{T}}, \tag{B.28}$$

$$\begin{aligned}\mathbf{K}_{\mathrm{M}}{}^{e4}_{ij} =& \alpha\mathbf{Q}(N_i\nabla_X)(N_j\nabla_X^{\mathrm{T}})\mathbf{Q}^{\mathrm{T}} + (\beta+\gamma)(N_j\nabla_X^{\mathrm{T}})(N_i\nabla_X)\mathbf{I} + (\beta-\gamma)\mathbf{Q}(N_j\nabla_X)(N_i\nabla_X^{\mathrm{T}})\mathbf{Q}^{\mathrm{T}} \\ &- (\mu+\nu)N_iN_j\left(\mathbf{F}\mathbf{F}^{\mathrm{T}} - \mathrm{tr}(\mathbf{F}\mathbf{F}^{\mathrm{T}})\mathbf{I}\right) + (\mu-\nu)N_iN_j\left[\mathbf{m_1}\ \mathbf{m_2}\ \mathbf{m_3}\right].\end{aligned} \tag{B.29}$$

Finally, the element stiffness matrix is the sum of geometric and material stiffness block matrices in the following form

$$\mathbf{K}^e = \begin{bmatrix} [\mathbf{K}_{\mathrm{M}}{}^e_{11}] + [\mathbf{K}_{\mathrm{G}}{}^e_{11}] & [\mathbf{K}_{\mathrm{M}}{}^e_{12}] + [\mathbf{K}_{\mathrm{G}}{}^e_{12}] & \cdots & [\mathbf{K}_{\mathrm{M}}{}^e_{1n}] + [\mathbf{K}_{\mathrm{G}}{}^e_{1n}] \\ [\mathbf{K}_{\mathrm{M}}{}^e_{21}] + [\mathbf{K}_{\mathrm{G}}{}^e_{21}] & [\mathbf{K}_{\mathrm{M}}{}^e_{22}] + [\mathbf{K}_{\mathrm{G}}{}^e_{22}] & \cdots & [\mathbf{K}_{\mathrm{M}}{}^e_{2n}] + [\mathbf{K}_{\mathrm{G}}{}^e_{2n}] \\ \vdots & \vdots & \ddots & \vdots \\ [\mathbf{K}_{\mathrm{M}}{}^e_{n1}] + [\mathbf{K}_{\mathrm{G}}{}^e_{n1}] & [\mathbf{K}_{\mathrm{M}}{}^e_{n2}] + [\mathbf{K}_{\mathrm{G}}{}^e_{n2}] & \cdots & [\mathbf{K}_{\mathrm{M}}{}^e_{nn}] + [\mathbf{K}_{\mathrm{G}}{}^e_{nn}] \end{bmatrix}, \tag{B.30}$$

where n in (B.30) represents the number of nodes on the element.

Appendix B.2. Matrix F^e

First we introduce the block matrix $\mathbf{F}_{aj}$ which is $[3 \times 6]$:

$$\mathbf{F}_{aj} = \Big\{ \lambda \mathbf{Q}(M_a \nabla_X)(N_j \nabla_X)^{\mathrm{T}} \mathbf{Q}^{\mathrm{T}} + (\mu+\nu)(N_j \nabla_X)^{\mathrm{T}}(M_a \nabla_X)\mathbf{I} + (\mu-\nu)\mathbf{Q}(N_j \nabla_X)(M_a \nabla_X)^{\mathrm{T}}\mathbf{Q}^{\mathrm{T}}, \quad -\widehat{\mathbf{QB}(M_a \nabla_X)} N_j + 2\lambda \mathbf{Q}(M_a \nabla_X)\boldsymbol{\ell}^{\mathrm{T}} N j + (\mu+\nu)\widehat{\mathbf{F}(M_a \nabla_X)} N_j - (\mu-\nu)\mathbf{Q}\mathbf{F}^{\mathrm{T}}\widehat{\mathbf{Q}(M_a \nabla_X)} N_j, \Big\} \tag{B.31}$$

$$\mathbf{F}_{aj}^{\mathrm{T}} = \left\{ \begin{array}{c} \lambda \mathbf{Q}(M_a \nabla_X)(N_j \nabla_X)^{\mathrm{T}} \mathbf{Q}^{\mathrm{T}} + (\mu+\nu)(N_j \nabla_X)^{\mathrm{T}}(M_a \nabla_X)\mathbf{I} + (\mu-\nu)\mathbf{Q}(N_j \nabla_X)(M_a \nabla_X)^{\mathrm{T}}\mathbf{Q}^{\mathrm{T}} \\ -\widehat{\mathbf{QB}(M_a \nabla_X)} N_j + 2\lambda \mathbf{Q}(M_a \nabla_X)\boldsymbol{\ell}^{\mathrm{T}} N j + (\mu+\nu)\widehat{\mathbf{F}(M_a \nabla_X)} N_j - (\mu-\nu)\mathbf{Q}\mathbf{F}^{\mathrm{T}}\widehat{\mathbf{Q}(M_a \nabla_X)} N_j, \end{array} \right\} \quad [6 \times 3], \tag{B.32}$$

where $\boldsymbol{\ell} = \mathrm{ax}(\mathrm{skew}(\mathbf{F}\mathbf{Q}^{\mathrm{T}}))$, giving the element matrix:

$$\mathbf{F}^e = \int_V \begin{bmatrix} \mathbf{F}_{11} & \mathbf{F}_{12} & \mathbf{F}_{13} & \mathbf{F}_{14} & \mathbf{F}_{15} & \mathbf{F}_{16} & \mathbf{F}_{17} & \mathbf{F}_{18} \\ \mathbf{F}_{21} & \mathbf{F}_{22} & \mathbf{F}_{23} & \mathbf{F}_{24} & \mathbf{F}_{25} & \mathbf{F}_{26} & \mathbf{F}_{27} & \mathbf{F}_{28} \\ \mathbf{F}_{31} & \mathbf{F}_{32} & \mathbf{F}_{33} & \mathbf{F}_{34} & \mathbf{F}_{35} & \mathbf{F}_{36} & \mathbf{F}_{37} & \mathbf{F}_{38} \end{bmatrix} dV, \quad [9 \times 48] \tag{B.33}$$

Appendix C. Implemented algorithm

In the 1st iteration ($k = 1$) we assume that the system is undeformed, i.e.

$$\mathbf{u}^{e^{(1)}} = \mathbf{0}, \qquad \mathbf{Q}^{e^{(1)}} = \mathbf{I}, \quad \boldsymbol{\alpha}^{e^{(1)}} = \mathbf{0} \quad \Rightarrow \quad \mathbf{F} = \mathbf{I}, \quad \mathbf{B} = \mathbf{0}, \quad \mathbf{G} = \mathbf{0}, \tag{C.1}$$

DO $k = 1, 2, ..., niter$:

- on the element level, given $\mathbf{u}^{e^{(k)}}$, $\mathbf{Q}^{e^{(k)}} = \left\{ q_0^{e^{(k)}}, \mathbf{q}^{e^{(k)}} \right\}$ compute $\boldsymbol{\alpha}^{e^{(k)}}$ using equation (32) as

$$\boldsymbol{\alpha}^{e^{(k)}} = \mathbf{H}^{e^{(k)^{-1}}} \left(\mathbf{r}^{\alpha, e^{(k)}} + \mathbf{q}^{ext, e, \alpha^{(k)}} - \tilde{\mathbf{F}}^{e^{(k)}} \mathbf{u}^{e^{(k)}} \right), \tag{C.2}$$

- from the linearization of the element residual force vector and the incompatible modes residual, for $\mathbf{g}^{e,\alpha}\left(\mathbf{u}^e, \mathbf{Q}^e, \boldsymbol{\alpha}^e\right) = \mathbf{0}$ we obtain

$$\mathbf{K}^{e^{(k)}} \Delta \mathbf{d}^{e^{(k)}} + \mathbf{F}^{e^{(k)^{\mathrm{T}}}} \Delta \boldsymbol{\alpha}^{e^{(k)}} = \mathbf{q}^{ext, e^{(k)}} - \mathbf{q}^{int, e^{(k)}}, \tag{C.3}$$

$$\mathbf{F}^{e^{(k)}} \Delta \mathbf{d}^{e^{(k)}} + \mathbf{H}^{e^{(k)}} \Delta \boldsymbol{\alpha}^{e^{(k)}} = \mathbf{0}, \tag{C.4}$$

- next we perform the static condensation of the linearized form by expressing $\Delta \boldsymbol{\alpha}^{e^{(k)}}$ from equation (C.4) as

$$\Delta \boldsymbol{\alpha}^{e^{(k)}} = -\mathbf{H}^{e^{(k)^{-1}}} \mathbf{F}^{e^{(k)}} \Delta \mathbf{d}^{e^{(k)}}, \tag{C.5}$$

and introduce it into the equation (C.3) to obtain

$$\left(\mathbf{K}^{e^{(k)}} - \mathbf{F}^{e^{(k)^{\mathrm{T}}}} \mathbf{H}^{e^{(k)^{-1}}} \mathbf{F}^{e^{(k)}} \right) \Delta \mathbf{d}^{e^{(k)}} = \mathbf{q}^{ext, e^{(k)}} - \mathbf{q}^{int, e^{(k)}}, \tag{C.6}$$

where $\tilde{\mathbf{K}}^{e^{(k)}} = \mathbf{K}^{e^{(k)}} - \mathbf{F}^{e^{(k)^{\mathrm{T}}}} \mathbf{H}^{e^{(k)^{-1}}} \mathbf{F}^{e^{(k)}}$ represents the condensed stiffness matrix.

- after static condesation of the incompatible-mode increment, we perform the standard finite element assembly procedure and compute displacement and rotation increments on the assembly level $\Delta\mathbf{d}^{(k)} = \left\langle \Delta\mathbf{u}^{(k)}\ \Delta\boldsymbol{\varphi}^{(k)} \right\rangle^{\mathrm{T}}$, which is then used to provide the updated values of displacements, rotations, strain tensor and curvature tensor

- update displacements:

$$\mathbf{u}^{(k+1)} := \mathbf{u}^{(k)} + \Delta\mathbf{u}^{(k)} \tag{C.7}$$

- update orientation matrix:

  In general, after obtaining the vector increment of the microrotation field $\Delta\boldsymbol{\varphi}^{(k)}$ in the k-th iteration we form the corresponding quaternion increment as

$$\mathbf{q}'^{(k)}_{\Delta\boldsymbol{\varphi}} = \left\{ q^{(k)}_{\Delta\varphi},\ \mathbf{q}^{(k)}_{\Delta\boldsymbol{\varphi}} \right\} = \left\{ \cos\left(\frac{\Delta\varphi^{(k)}}{2}\right), \frac{\sin\left(\frac{\Delta\varphi^{(k)}}{2}\right)}{\Delta\varphi^{(k)}} \Delta\boldsymbol{\varphi}^{(k)} \right\}, \tag{C.8}$$

  where $\Delta\varphi^{(k)}$ represents the norm of vector $\Delta\boldsymbol{\varphi}^{(k)}$, i.e. $\Delta\varphi^{(k)} = \sqrt{\Delta\boldsymbol{\varphi}^{(k)} \cdot \Delta\boldsymbol{\varphi}^{(k)}}$. The quaternion update is defined through the quaternion multiplication, i.e.

$$\mathbf{q}'^{(k+1)} = \mathbf{q}'^{(k)}_{\Delta\boldsymbol{\varphi}} \circ \mathbf{q}'^{(k)} = \left\{ q_0^{(k+1)},\ \mathbf{q}^{(k+1)} \right\}, \tag{C.9}$$

  where $\mathbf{q}'^{(k)} = \left\{ q_0^{(k)},\ \mathbf{q}^{(k)} \right\}$ is the quaternion obtained in the previous ($k-$th) iteration. The updated quaternion is obtained as [20]

$$\mathbf{q}'^{(k+1)} = \left\{ q^{(k)}_{\Delta\varphi} \cdot q^{(k)}_0 - \mathbf{q}^{(k)}_{\Delta\boldsymbol{\varphi}} \cdot \mathbf{q}^{(k)},\ \mathbf{q}^{(k)}_{\Delta\boldsymbol{\varphi}} \times \mathbf{q}^{(k)} + q^{(k)}_0 \cdot \mathbf{q}^{(k)}_{\Delta\boldsymbol{\varphi}} + q^{(k)}_{\Delta\varphi} \cdot \mathbf{q}^{(k)} \right\}. \tag{C.10}$$

  Next, we form the updated orientation matrix $\mathbf{Q}_{\mathrm{new}}$ as

$$\mathbf{Q}_{\mathrm{new}} = (2q_0^{(k+1)^2} - 1)\mathbf{I} + 2q_0^{(k+1)}\widehat{\mathbf{q}^{(k+1)}} + 2\mathbf{q}^{(k+1)} \otimes \mathbf{q}^{(k+1)}. \tag{C.11}$$

- update Biot-like strain tensor $\mathbf{E}$:

In order to update the Biot-like strain and curvature tensors $\mathbf{E}$ and $\mathbf{K}$ we have to compute the values of the displacement field and orientation matrix at the integration points. For the deformation gradient $\mathbf{F}$, these values are easily obtained by finding the derivative of the interpolated values in the corresponding Gauss point l as follows:

$$\mathbf{F} = \mathbf{I} + \mathrm{GRAD}\left(\sum_{j=1}^{n_{node}} N_i(\xi_l,\eta_l,\zeta_l)\mathbf{u}_i + \sum_{a=1}^{3} M_a(\xi_l,\eta_l,\zeta_l)\boldsymbol{\alpha}_a\right) \tag{C.12}$$

$$= \mathbf{I} + \sum_{j=1}^{n_{node}} \begin{Bmatrix} u_{i1} \\ u_{i2} \\ u_{i3} \end{Bmatrix} \otimes \begin{Bmatrix} \frac{\partial N_i(\xi_l,\eta_l,\zeta_l)}{\partial X_1} \\ \frac{\partial N_i(\xi_l,\eta_l,\zeta_l)}{\partial X_2} \\ \frac{\partial N_i(\xi_l,\eta_l,\zeta_l)}{\partial X_3} \end{Bmatrix} + \sum_{a=1}^{3} \begin{Bmatrix} \alpha_{a1} \\ \alpha_{a2} \\ \alpha_{a3} \end{Bmatrix} \otimes \begin{Bmatrix} \frac{\partial M_a(\xi_l,\eta_l,\zeta_l)}{\partial X_1} \\ \frac{\partial M_a(\xi_l,\eta_l,\zeta_l)}{\partial X_2} \\ \frac{\partial M_a(\xi_l,\eta_l,\zeta_l)}{\partial X_3} \end{Bmatrix}, \tag{C.13}$$

and the values of the orientation matrix are obtained as $\mathbf{Q} = \exp(\widehat{\Delta\boldsymbol{\varphi}})\mathbf{Q}_{\mathrm{old}}$ where $\mathbf{Q}_{\mathrm{old}}$ represents the orientation matrix in the previous iteration. Then, the current strain tensor is evaluated by substituting the obtained matrices $\mathbf{F}$ and $\mathbf{Q}$ into equation (4).

- update Biot-like curvature tensor $\mathbf{K}$:

In order to update the curvature tensor, we start by extracting the curvature vector $\mathbf{K}_i$ from $\mathbf{K} = [\mathbf{K}_1\ \mathbf{K}_2\ \mathbf{K}_3]$. The curvature vector $\mathbf{K}_i$ is defined as

$$\mathbf{K}_i = \mathrm{ax}(\widehat{\mathbf{K}_i}) = \mathrm{ax}\left(\mathbf{Q}^{\mathrm{T}}\frac{\partial \mathbf{Q}}{\partial X_i}\right). \tag{C.14}$$

Next, we substitute $\mathbf{Q} = \exp(\widehat{\Delta\boldsymbol{\varphi}})\mathbf{Q}_{\mathrm{old}}$ into $\widehat{\mathbf{K}_i} = \mathbf{Q}^{\mathrm{T}}\frac{\partial \mathbf{Q}}{\partial X_i}$ and obtain

$$\widehat{\mathbf{K}_i} = \mathbf{Q}_{\mathrm{old}}^{\mathrm{T}}\exp(\widehat{\Delta\boldsymbol{\varphi}})^{\mathrm{T}}\frac{\partial\left(\exp(\widehat{\Delta\boldsymbol{\varphi}})\mathbf{Q}_{\mathrm{old}}\right)}{\partial X_i}.$$

We further obtain

$$\widehat{\mathbf{K}_i} = \mathbf{Q}_{\mathrm{old}}^{\mathrm{T}}\exp(\widehat{\Delta\boldsymbol{\varphi}})^{\mathrm{T}}\frac{\partial\exp(\widehat{\Delta\boldsymbol{\varphi}})}{\partial X_i}\mathbf{Q}_{\mathrm{old}} + \mathbf{Q}_{\mathrm{old}}^{\mathrm{T}}\underbrace{\exp(\widehat{\Delta\boldsymbol{\varphi}})^{\mathrm{T}}\exp(\widehat{\Delta\boldsymbol{\varphi}})}_{\mathbf{I}}\frac{\partial\mathbf{Q}_{\mathrm{old}}}{\partial X_i}.$$

Here, we recognize that $\mathbf{Q}_{\text{old}}^{\text{T}}\dfrac{\partial \mathbf{Q}_{\text{old}}}{\partial X_i} = \widehat{\mathbf{K}}_{i\text{old}}$ and obtain

$$\widehat{\mathbf{K}_i} = \mathbf{Q}_{\text{old}}^{\text{T}}\text{exp}(\widehat{\Delta\boldsymbol{\varphi}})^{\text{T}}\frac{\partial \text{exp}(\widehat{\Delta\boldsymbol{\varphi}})}{\partial X_i}\mathbf{Q}_{\text{old}} + \widehat{\mathbf{K}}_{i\text{old}}.$$

Next, we rewrite $\mathbf{Q}_{\text{old}} = \text{exp}(\widehat{\Delta\boldsymbol{\varphi}})^{\text{T}}\mathbf{Q}$ and obtain

$$\begin{aligned}\widehat{\mathbf{K}_i} &= \mathbf{Q}^{\text{T}}\underbrace{\text{exp}(\widehat{\Delta\boldsymbol{\varphi}})\text{exp}(\widehat{\Delta\boldsymbol{\varphi}})^{\text{T}}}_{\mathbf{I}}\frac{\partial \text{exp}(\widehat{\Delta\boldsymbol{\varphi}})}{\partial X_i}\text{exp}(\widehat{\Delta\boldsymbol{\varphi}})^{\text{T}}\mathbf{Q} + \widehat{\mathbf{K}}_{i\text{old}} \\ &= \mathbf{Q}^{\text{T}}\frac{\partial \text{exp}(\widehat{\Delta\boldsymbol{\varphi}})}{\partial X_i}\text{exp}(\widehat{\Delta\boldsymbol{\varphi}})^{\text{T}}\mathbf{Q} + \widehat{\mathbf{K}}_{i\text{old}}.\end{aligned}$$

After a lengthy, but otherwise straightforward algebraic manipulation of the term $\dfrac{\partial \text{exp}(\widehat{\Delta\boldsymbol{\varphi}})}{\partial X_i}\text{exp}(\widehat{\Delta\boldsymbol{\varphi}})^{\text{T}}$ (presented in detail in [29]) we obtain

$$\begin{aligned}\widehat{\mathbf{K}_i} &= \mathbf{Q}^{\text{T}}\widehat{\mathbf{H}(\Delta\boldsymbol{\varphi})\frac{\partial \Delta\boldsymbol{\varphi}}{\partial X_i}}\mathbf{Q} + \widehat{\mathbf{K}}_{i\text{old}} \\ &= \widehat{\mathbf{K}}_{i\text{old}} + \Delta\widehat{\mathbf{K}}_i,\end{aligned} \tag{C.15}$$

where

$$\mathbf{H}(\Delta\boldsymbol{\varphi}) = \mathbf{I} + \frac{1-\cos(\Delta\varphi)}{(\Delta\varphi)^2}\widehat{\Delta\boldsymbol{\varphi}} + \frac{\Delta\varphi - \sin(\Delta\varphi)}{(\Delta\varphi)^3}\widehat{\Delta\boldsymbol{\varphi}}^2, \tag{C.16}$$

and $\Delta\varphi$ represents the norm of the iterative change in the microrotation vector. Finally, by using the identity $\widehat{\mathbf{Q}\mathbf{v}} = \mathbf{Q}\hat{\mathbf{v}}\mathbf{Q}^{\text{T}}\ \forall\ \mathbf{v} \in \mathbb{R}^3,\ \mathbf{Q} \in \text{SO}(3)$, we obtain the update of the material curvature vector as

$$\mathbf{K}_i = \mathbf{Q}^{\text{T}}\mathbf{H}(\Delta\boldsymbol{\varphi})\frac{\partial \Delta\boldsymbol{\varphi}}{\partial X_i} + \mathbf{K}_{i\text{old}}. \tag{C.17}$$

Finally, the update of the curvature tensor can be regarded as the update of the three curvature vectors, i.e. $\mathbf{K} = [\mathbf{K}_1\ \mathbf{K}_2\ \mathbf{K}_3]$ where

$$\mathbf{K}_1 = \mathbf{Q}^{\text{T}}\mathbf{H}(\Delta\boldsymbol{\varphi})\frac{\partial \Delta\boldsymbol{\varphi}}{\partial X_1} + \mathbf{K}_{1\text{old}},\ \ \mathbf{K}_2 = \mathbf{Q}^{\text{T}}\mathbf{H}(\Delta\boldsymbol{\varphi})\frac{\partial \Delta\boldsymbol{\varphi}}{\partial X_2} + \mathbf{K}_{2\text{old}},\ \ \mathbf{K}_3 = \mathbf{Q}^{\text{T}}\mathbf{H}(\Delta\boldsymbol{\varphi})\frac{\partial \Delta\boldsymbol{\varphi}}{\partial X_3} + \mathbf{K}_{3\text{old}}, \tag{C.18}$$

which can be written as

$$\begin{aligned}\mathbf{K} &= \mathbf{K}_{\text{old}} + \Delta\mathbf{K} \\ &= \mathbf{K}_{\text{old}} + \mathbf{Q}^{\text{T}}\mathbf{H}(\Delta\boldsymbol{\varphi})\text{GRAD}(\Delta\boldsymbol{\varphi}).\end{aligned} \tag{C.19}$$

- compute the residual for updated values and test convergence on the assembly level:

$$\begin{aligned} &\text{IF } ||\mathbf{g}|| \leq 10^{-16} \Rightarrow \text{CONVERGED SOLUTION} \\ &\text{ELSE } \Rightarrow \text{NEXT ITERATION} \end{aligned} \tag{C.20}$$

References

[1] R S Lakes. Size effects and micromechanics of a porous solid. *Journal of Materials Science*, 18:2572–2580, 1983.

[2] R Lakes. Experimental methods for study of Cosserat elastic solids and other generalized elastic continua. *Continuum Models for Materials with Micro-structure*, (1):1–22, 1996.

[3] R S Lakes. Physical Meaning of Elastic Constants in Cosserat, Void, and Microstretch Elasticity. *Mechanics of Materials and Structures*, 11(3):1–13, 2016.

[4] E Cosserat and F Cosserat. *Théorie des corps déformables*. Herman, Paris, 1909.

[5] W Nowacki. *Theory of micropolar elasticity*. Springer-Verlag, Vienna, 1972.

[6] J Dyszlewicz. *Micropolar Theory of Elasticity*. Springer-Verlag Berlin and Heidelberg GmbH & Co. KG, Berlin, 2004.

[7] A C Eringen. Linear Theory of Micropolar Elasticity. *Journal of Mathematics and Mechanics*, 15:909–923, 1966.

[8] R D Gauthier and W E Jahsman. A Quest for Micropolar Elastic Constants. *Journal of Applied Mechanics*, 42(2):369–374, 1975.

[9] S Nakamura, R Benedict, and R Lakes. Finite element method for orthotropic micropolar elasticity. *International Journal of Engineering Science*, 22(3):319–330, 1984.

[10] E Providas and M A Kattis. Finite element method in plane Cosserat elasticity. *Computers and Structures*, 80(27-30):2059–2069, 2002.

[11] S Hassanpour and G R Heppler. Micropolar elasticity theory: a survey of linear isotropic equations, representative notations, and experimental investigations. *Mathematics and Mechanics of Solids*, 22(2):224–242, 2015.

[12] S Grbčić, A Ibrahimbegović, and G Jelenić. Variational formulation of micropolar elasticity using 3D hexahedral finite-element interpolation with incompatible modes. *Computers and Structures*, 205:1–14, aug 2018.

[13] A C Eringen. *Microcontinuum Field Theories: I. Foundations and Solids*. Springer-Verlag, New York, 2012.

[14] P Steinmann. A micropolar theory of finite deformation and finite rotation multiplicative elastoplasticity. *International Journal of Solids and Structures*, 31(8):1063–1084, 1994.

[15] W Pietraszkiewicz and V A Eremeyev. On natural strain measures of the non-linear micropolar continuum. *International Journal of Solids and Structures*, 46(3-4):774–787, 2009.

[16] L Obrezkov, M K Matikainen, and R Kouhia. Micropolar beam-like structures under large deformation. *International Journal of Solids and Structures*, 254-255:111899, nov 2022.

[17] S Bauer, M Schäfer, P Grammenoudis, and Ch. Tsakmakis. Three-dimensional finite elements for large deformation micropolar elasticity. *Computer Methods in Applied Mechanics and Engineering*, 199(41-44):2643–2654, 2010.

[18] S Grbčić Erdelj, G Jelenić, and A Ibrahimbegović. Geometrically non-linear 3D finite-element analysis of micropolar continuum. *International Journal of Solids and Structures*, 202:745–764, 2020.

[19] A Ibrahimbegović. *Nonlinear Solid Mechanics: Theoretical Formulations and Finite Element Solution Methods*. Springer, London, 2009.

[20] I Kožar and A Ibrahimbegović. Finite element formulation of the finite rotation solid element. *Finite Elements in Analysis and Design*, 20(2):101–126, jun 1995.

[21] S Grbčić. *Linked interpolation and strain invariance in finite-element modelling of micropolar continuum*. PhD thesis, University of Rijeka and Université de Technologie de Compiègne – Sorbonne Universités, 2018.

[22] Brian C. Hall. *Lie Groups, Lie Algebras, and Representations*, volume 222 of *Graduate Texts in Mathematics*. Springer International Publishing, Cham, 2015.

[23] E Reissner. On one-dimensional finite-strain beam theory: The plane problem. *Zeitschrift für angewandte Mathematik und Physik ZAMP*, 23(5):795–804, sep 1972.

[24] A Ibrahimbegovic and E L Wilson. A modified method of incompatible modes. *Communications in Applied Numerical Methods*, 7(3):187–194, 1991.

[25] R L Taylor. FEAP - Finite Element Analysis Program, 2014.

[26] G Jelenić. Pure bending in non-linear micropolar elasticity. *International Journal of Mechanics and Materials in Design*, 18(1):243–265, 2022.

[27] S Grbčić, G Jelenić, and D Ribarić. Quadrilateral 2D linked-interpolation finite elements for micropolar continuum. *Acta Mechanica Sinica/Lixue Xuebao*, 35(5):1001–1020, oct 2019.

[28] K J Bathe and S Bolourchi. Large displacement analysis of three-dimensional beam structures. *International Journal for Numerical Methods in Engineering*, 14(7):961–986, jan 1979.

[29] M Gaćeša. *Fixed-Pole Concept in 3D Beam Finite Elements - Relationship to Standard Approaches and Analysis of Different Interpolations*. PhD thesis, University of Rijeka, Faculty of Civil Engineering, 2015.